Monthly Notices
of the
ROYAL ASTRONOMICAL SOCIETY

MNRAS **484,** 5530–5550 (2019)
Advance Access publication 2019 January 5

doi:10.1093/mnras/stz003

A deep view of a fossil relic in the Galactic bulge: the Globular Cluster HP 1

L. O. Kerber [1,2★] M. Libralato [3,4,5] S. O. Souza,[1] R. A. P. Oliveira [1] S. Ortolani,[4,5] A. Pérez-Villegas [1] B. Barbuy,[1] B. Dias,[6,7] E. Bica[8] and D. Nardiello [4,5]

[1] *Universidade de São Paulo, IAG, Rua do Matão 1226, Cidade Universitária, São Paulo 05508-900, Brazil*
[2] *Universidade Estadual de Santa Cruz, Rodovia Jorge Amado km 16, Ilhéus 45662-000, Bahia, Brazil*
[3] *Space Telescope Science Institute, 3700 San Martin Drive, Baltimore, MD 21218, USA*
[4] *Dipartimento di Fisica e Astronomia, Università di Padova, I-35122 Padova, Italy*
[5] *INAF-Osservatorio Astronomico di Padova, Vicolo dell'Osservatorio 5, I-35122 Padova, Italy*
[6] *European Southern Observatory, Alonso de Cordova 3107, Santiago, Chile*
[7] *Departamento de Física, Facultad de Ciencias Exactas, Universidad Andrés Bello, Av. Fernandez Concha 700, Las Condes, Santiago, Chile*
[8] *Universidade Federal do Rio Grande do Sul, Departamento de Astronomia, CP 15051, Porto Alegre 91501-970, Brazil*

Accepted 2018 December 10. Received 2018 November 14; in original form 2018 May 8

ABSTRACT

HP 1 is an α-enhanced and moderately metal-poor bulge globular cluster with a blue horizontal branch. These combined characteristics make it a probable relic of the early star formation in the innermost Galactic regions. Here, we present a detailed analysis of a deep near-infrared (NIR) photometry of HP 1 obtained with the NIR GSAOI + GeMS camera at the Gemini-South telescope. J and K_S images were collected with an exquisite spatial resolution (FWHM $\sim$0.1 arcsec), reaching stars at two magnitudes below the MSTO. We combine our GSAOI data with archival F606W-filter *HST* ACS/WFC images to compute relative proper motions and select bona fide cluster members. Results from statistical isochrone fits in the NIR and optical-NIR colour–magnitude diagrams indicate an age of $12.8^{+0.9}_{-0.8}$ Gyr, confirming that HP 1 is one of the oldest clusters in the Milky Way. The same fits also provide apparent distance moduli in the K_S and V filters in very good agreement with the ones from 11 RR Lyrae stars. By subtracting the extinction in each filter, we recover a heliocentric distance of $6.59^{+0.17}_{-0.15}$ kpc. Furthermore, we refine the orbit of HP 1 using this accurate distance and update and accurate radial velocities (from high-resolution spectroscopy) and absolute proper motions (from *Gaia* DR2), reaching mean perigalactic and apogalactic distances of $\sim$0.12 and $\sim$3 kpc, respectively.

Key words: instrumentation: adaptive optics – Galaxy: bulge – globular clusters: individual: HP 1 – infrared: stars.

1 INTRODUCTION

Galactic globular clusters (GCs) play a key role in the understanding of the formation history of the Milky Way (MW) because they are excellent tracers of its early chemical evolution, going from the outer halo to the innermost Galactic regions. In particular, a very interesting class of objects are the bulge GCs possessing moderately metal-poor ([Fe/H] $\lesssim -1.0$) and α-enhanced ([α/Fe] $\gtrsim +0.3$) stars, with a blue horizontal branch (BHB). The relatively high metallicity of these GCs is due to an early fast chemical enrichment in the central parts of the MW as shown by Cescutti et al. (2008). These objects might be relics of an early generation of long-lived stars formed in the proto-Galaxy. A dozen of them were identified by Barbuy, Bica & Ortolani (1998) and Barbuy et al. (2009), and for this reason we have been performing high-resolution spectroscopy studies (Barbuy et al. 2006, 2007, 2009, 2014, 2016, 2018), as well as optical and near-infrared (NIR) multiepoch photometry to build proper-motion (PM) cleaned colour–magnitude diagrams (CMDs; e.g. Ortolani et al. 2011; Rossi et al. 2015). Recently, this hypothesis has been tested for two bulge GCs, NGC 6522, and NGC 6626, employing a statistical isochrone fitting method on deep and decontaminated *Hubble Space Telescope* (*HST*) optical CMDs, confirming that these clusters are old with a range of ages between $\sim$12.5 and 13.0 Gyr (Kerber et al. 2018).

★ E-mail: lokerber@uesc.br

Age derivation for a larger sample of bulge GCs in order to test the initial hypothesis concerning their very old ages is however made difficult, due to the severe extinction, strong field contamination, and relatively large distance. The bulge GCs represent therefore a last frontier in terms of observational challenge to study such objects in the Galaxy. Furthermore, the total mass of a bulge GC in only a few cases surpasses $\sim 10^5\,M_\odot$, making the disentanglement between cluster and field exclusively possible with PM cleaning techniques. In fact, even with the exquisite spatial resolution and accurate photometry from the *HST*, it is not an easy task to build deep PM-cleaned CMDs in the UV/visual for bulge GCs. Not by chance, the two most comprehensive *HST* surveys of GCs – the Advanced Camera for Surveys (ACS) survey of GCs (Sarajedini et al. 2007) and the *HST* UV Legacy Survey of GCs (Piotto et al. 2015) – were focused on halo and disc objects, almost neglecting those in the bulge.

NIR is the natural solution to go deep in the stellar content of the bulge GCs. Using longer wavelengths than in the visible, the extinction is dramatically reduced (e.g. $A_{K_S} \sim 0.12 A_V$) and the adaptive optics (AO) is significantly more efficient, reaching almost the telescope diffraction limit (full-width at half maximum, FWHM, ∼0.1 arcsec).

Boosted by the continuing improvement of the third generation of infrared detectors based on HgCdTe technology in the last two decades, significant efforts have been done to collect NIR photometry of bulge GCs. Notably, projects using ground-based 2–4 m class telescopes from the European Southern Observatory (ESO; e.g. Valenti, Ferraro & Origlia 2007, 2010), particularly the *Vista Variable in the Via Láctea* (VVV) Survey (e.g. Minniti et al. 2010, 2017; Cohen et al. 2017), have expanded our knowledge about these objects by covering almost all stars in the red giant branch (RGB) and horizontal branch (HB) in different filters. In combination with several spectroscopy studies, in particular those based on high-resolution spectroscopy of individual red giants in the visible (e.g. Barbuy et al. 2014; Gratton et al. 2015; Muñoz et al. 2017; Villanova et al. 2017) and in the NIR (e.g. Lee, Carney & Balachandran 2004; Origlia & Rich 2004; Valenti et al. 2011; Schiavon et al. 2017), important results to establish a more comprehensive scenario for the formation and evolution of the bulge GCs has been obtained. This includes the metallicity distribution and chemical abundances analysis.

However, the lack of deep NIR photometry reaching at least one magnitude below the main-sequence turn-off (MSTO) of the bulge GCs has severely hampered the determination of reliable ages for these systems, therefore preventing the achievement of the age–metallicity relation (AMR) for the innermost Galactic region. Fortunately, the immediate perspective to overcome this challenge is positive thanks to the current NIR detector on board of the *HST* (the NIR channel of the Wide Field Camera 3 – WFC3/IR) and the multiconjugate adaptive optics systems (MCAO) at the large ground-based telescopes (e.g. Ferraro et al. 2016).

Recently, Cohen et al. (2018) presented deep NIR and optical-NIR CMDs for 16 bulge GCs built with *HST* photometry from WFC3/IR and ACS/Wide Field Channel (WFC) images. These homogeneous and high-quality data for a significant number of clusters, which includes HP 1, represent an important milestone for any future study concerning bulge GCs. Furthermore, recent NIR images using MCAO systems, such as the Multi-Conjugate Adaptive Optics Demonstrator (MAD) at the Very Large Telescope (VLT), and the Gemini South Adaptive Optics Imager (GSAOI) combined with the Gemini Multi-Conjugated Adaptive Optics System (GeMS) at the Gemini South Telescope, provided unprecedented results related to GCs (e.g. Turri et al. 2015; Massari et al. 2016a), specifically to the ones presented in the bulge (Saracino et al. 2015, 2016).

We obtained observing time at the Gemini South Telescope to collect deep J and K_S images of HP 1 using the GSAOI + GeMS camera. HP 1 is an inner bulge GC placed at just 3.33° from the Galactic Centre, with Galactic coordinates $l = -2.58°$, $b = +2.12°$ (Harris 1996). A metallicity of $[Fe/H] = -1.06 \pm 0.10$ was determined by the analysis of high-resolution spectra of eight red giant stars (Barbuy et al. 2006, 2016), in good agreement with results from low-resolution spectroscopy of $[Fe/H] = -1.17 \pm 0.07$ by Dias et al. (2016a). In addition, all these studies indicated that HP 1 is α-enhanced, with $[\alpha/Fe] \sim +0.3$. Previously, Ortolani et al. (2011) built a K_S versus $V - K_S$ PM cleaned CMD for HP 1, using two-epoch photometry separated by 14.25 yr, the first (in V) collected in 1994 with the NTT telescope and the second (in J and K_S) obtained in 2008 with the MAD at the VLT. This CMD of excellent quality, confirmed the presence of a BHB, but barely reached the MSTO ($K_S \sim 17.5$). Their analysis pointed out to a very old age (∼13.7 Gyr) and a metallicity of $[Fe/H] \sim -1.0$ (estimated from the RGB slope).

The main goal of this work is to check if HP 1 is a fossil relic. For this purpose, we used the aforementioned GSAOI+GeMS data in combination with *HST* images obtained with the ACS/WFC in F606W filter to compute relative PMs and isolate probable cluster members to plot in NIR and optical-NIR CMDs. RR Lyrae stars presented in the OGLE Collection of Variable Stars (CVS) for the Galactic bulge (Soszyński et al. 2014),[1] and the ($m_{F606W} - K_S$) versus ($J - K_S$) colour–colour diagram were used to provide additional constraints for the heliocentric distance, reddening, and helium abundance. Furthermore, we performed an orbital analysis of HP 1 using the cluster distance derived in this work, the recent and accurate radial velocities from high-resolution spectroscopy (Barbuy et al. 2016), and the absolute PMs from the *Gaia* DR2 catalogue (Gaia Collaboration et al. 2018), with the purpose of constraining the maximum Galactocentric distance where these fossil relic stars could be found.

This work is structured as follow. The Gemini and *HST* data are presented in Section 2, whereas CMDs and the relative PM computation are described in Section 3. In Section 4, the adopted stellar evolutionary models are indicated. Section 5 is dedicated to the colour–colour diagram and the RR Lyrae stars. Then, the statistical isochrone fitting method following a Bayesian approach and its results are reported in Sections 6 and 7. A discussion about age and distance determinations is in Section 8. We also present an orbital analysis of HP 1 in Section 9. Finally, conclusions and some perspectives are drawn in Section 10.

2 OBSERVATIONS

2.1 GSAOI+GeMS@Gemini-South

GSAOI is a mosaic of four Rockwell Hawaii-2RG 2048 × 2048 pixel^2 detectors that cover a field of view (FoV) of about 85 × 85 arcsec^2 on the sky. The pixel scale of the detectors is 20 mas pixel^{-1}.

The GSAOI observations of HP 1 analysed in this work were obtained on 2017 May 4 as part of the programme GS-2017A-Q44 (PI: L. Kerber). The field was observed in J and K_S filters with 14 images of exposure time of 30 s (DIT × NDIT = 30 s × 1) per filter.

[1] http://ogledb.astrouw.edu.pl/~ogle/CVS/

Five additional K_S-filter images with an exposure time of 10 s were achieved to extend the analysis to bright stars otherwise saturated in longer exposures. Fig. 1 presents the mosaic of GSAOI + GeMS K_S images for HP 1 used in this work, and a comparison between a GSAOI@Gemini-South and a MAD@VLT image.

The median value of the FWHM for J and K_S images is about 0.15 and 0.10 arcsec, respectively. The FWHM of J images is overall more stable than that of K_S exposures, which for the latter filter can be as large as 0.15 arcsec in the rightmost edges of chips 1 and 4 (see also the Appendix). As such, the quality of the data varies across the FoV. Furthermore, J-filter images are shallower than those in K_S, and limited our investigation of the MS of HP 1 to about one magnitude below the MSTO.

The reduction of GSAOI data was performed as in Libralato et al. (2014, 2015), following the procedures and softwares described in Anderson et al. (2006). We refer to these papers for the detailed description of the data reduction. Here, we provide a brief overview and discuss in detail the differences with respect to the reference papers.

For each chip, we created a hot-pixel mask following the prescriptions given by the official GSAOI website.[2] We adopted the most-recent dark frames available in the archive with an exposure time as close as possible to that of the scientific exposures. Hot-pixel structures change over time; therefore, our hot-pixel masks represent an average snapshot of the hot-pixel distribution in our scientific images.

Then, we constructed a master flat-field frame for each chip and filter. Flat-field exposures can be obtained with ('DOME FLAT ON') or without ('DOME FLAT OFF') flat-field light. The latter images are useful to estimate the amount of thermal emission of the telescope in H and K_S observations. The master flat-field images were obtained by computing the normalized σ-clipped median value of each pixel of the 'DOME FLAT ON' flat-field exposures. For K_S-filter frames, we subtracted in each flat-field image the median value of the K_S-filter 'DOME FLAT OFF' frames before combining them in a master flat-field image. In addition, flat-field exposures allowed us to create a map of bad-pixels in the detector.

We corrected scientific images by means of these master flat-field frames. We did not subtract any dark frame from our images because of the negligible amount of dark current in GSAOI detectors. Then, we flagged hot, bad and saturated pixels not to use them in the subsequent analysis. Saturation was set to 32 000 counts. Finally, we computed the median sky values in a 5 × 5 grid and subtracted the sky contribution in a given pixel of the detector according to this table.

We constructed a 5 × 5 array of empirical, spatially varying point-spread functions (PSFs) for each chip/exposure/filter based on the available bright and relatively isolated stars available in each image. PSFs were computed with the software `img2psf_GSAOI`, a modified version of the original `img2psf_WFI` made by Anderson et al. (2006). These empirical PSFs were used to measure position and flux of all detectable sources in the field. As a diagnostic parameter for the PSF fit, we defined the 'quality-of-PSF-fit' (`QFIT`) as the absolute fractional error in the PSF fit to the star (Anderson et al. 2008b). The `QFIT` value ranges between 0 and 1: the closer to 0, the better the PSF fit. Stellar positions were corrected for geometric distortion (GD). We refer to the Appendix for the detailed description of the GD solution of GSAOI detectors.

For each filter, we cross-identified the same stars in the meta catalogues (see the Appendix) to create a common reference frame with average positions and fluxes of all sources. The final GSAOI catalogue contains only stars measured in at least three K_S- and J-filter exposures. Photometry was calibrated to the Two Micron All Sky Survey (2MASS; Skrutskie et al. 2006) photometric system by using the MAD catalogue of Ortolani et al. (2011).

2.2 *HST*

We made use of *HST* data obtained in August 2016 with the ACS/WFC camera under GO-14074 (PI: Cohen; see Cohen et al. 2018) to compute relative PMs. The data set consists in four long (495 s) and one short (40 s) F606W-filter exposures. NIR images obtained with the IR channel of the Wide-Field Camera 3 (WFC3) are also available for this cluster. However, we chose not to use them because of the worse astrometric precision of WFC3/IR data with respect to that of ACS/WFC.

We used ACS/WFC `_flc` exposures, `_flt` images pipeline corrected for charge-transfer-efficiency (CTE) defects (see Anderson & Bedin 2010). Positions and fluxes of all stars in each image were extracted with a single finding wave by fitting empirical, spatially-, and time-varying PSFs obtained by tailoring the publicly available[3] library PSFs for each ACS/WFC F606W-filter exposure. Stellar positions were corrected for GD by using the GD solution provided by Anderson & King (2006). Finally, as for GSAOI data, we computed a master frame catalogue by means of six-parameter linear transformations. The ACS/WFC F606W photometry was registered on the Vega mag system as in, e.g., Bellini et al. (2017a).

3 PM-CLEANED CMDS

Field contamination in the CMD of HP 1 represents a major limitation for the analysis of this bulge GC, in particular along the MS. Therefore, we computed the relative PMs of the objects in the FoV by combining the GSAOI and *HST* catalogues, which offer a temporal baseline of 0.71 yr.

We applied local transformations to compute relative PMs similarly to Massari et al. (2013, see also Anderson et al. 2006). For each star in our GSAOI catalogue, we selected a sample of bright, well-measured, close-by likely cluster stars to compute the coefficients of the six-parameter linear transformations (rigid shifts in the two coordinates, one rotation, one change of scale, one term that represents the deviation from orthogonality between the two axes, and one term that accounts for the change of the relative scale between the two axes) to transform the position of the target star, as measured in the *HST* catalogue to the GSAOI reference frame. The relative displacement of a given star is computed as the difference between its GSAOI-based and the *HST*-based transformed positions on the GSAOI reference-frame system. The relative PM errors are estimated as the sum in quadrature of the positional uncertainty in the GSAOI and *HST* catalogues (in mas) divided by the temporal baseline. We computed the PMs in relative terms. As such, the distribution of HP 1 stars is centred on the origin of the vector-point diagram (VPD), while field stars lie in different locations according to their relative motion with respect to HP 1.

We found colour-related and spatial systematic effects in our final relative PMs; therefore, we corrected them similarly to Anderson et al. (2006) and Bellini et al. (2018), respectively. Finally, we

[2] https://www.gemini.edu/sciops/instruments/gsaoi/

[3] http://www.stsci.edu/~jayander/STDPSFs/

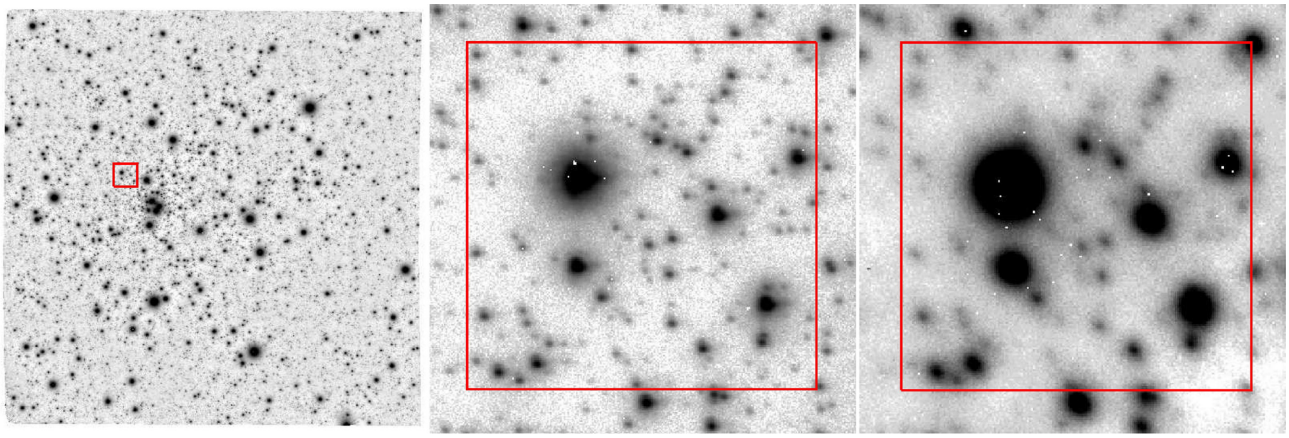

Figure 1. FoV of HP 1. The mosaic of the K_S-filter GSAOI images used in this paper is shown in the left-hand panel. The FoV covered is about 1.4 × 1.5 arcmin^2. In the middle and right panels, we present a comparison between a GSAOI@Gemini-S and MAD@VLT exposure in a 5 × 5 arcsec^2 box. Images are in logarithmic scale; north is up and east to the left.

used the *Gaia* Data Release 1 (Gaia Collaboration et al. 2016a,b) catalogue to transform our relative PMs from GSAOI pixels year^{-1} into $\mu_\alpha \cos\delta$ and μ_δ relative PMs in mas yr^{-1}.

In Fig. 2, we show the K_S versus $(J - K_S)$ CMDs and VPDs. In this and all other figures of the paper, CMDs are corrected for the effects of the differential reddening as described in Bellini et al. (2017b), which is grounded on the methodology described in Milone et al. (2012). We refer to these papers for the detailed description of the correction. Furthermore, in all CMDs we present only well-measured stars, defined as having: (i) x and y positional rms, (ii) K_S and J magnitude rms, (iii) K_S and J QFIT, and (iv) one-dimensional relative PM error smaller than the 75th-percentile value at any given magnitude. Most of the rejected stars are at the faint end of the MS and in regions imaged in chips 1 and 4 because of the worse quality of the data (see Section 2.1).

The left-hand panel of Fig. 2 shows the CMD of all objects, while the two rightmost panels show likely cluster members and field objects, respectively. The VPDs illustrate the membership-selection criteria we adopted to identify bona fide cluster members. We divided our sample in six magnitude bins of 1.5 magnitudes each. In each bin, we drew a circle centred in the origin of the VPD (the mean motion of HP 1, by construction). All stars enclosed by the circles are considered members of HP 1. The selection radius adopted in each magnitude bin was chosen as a compromise between including field stars with a motion similar to that of the cluster, and excluding HP 1 members with a large relative PM. Furthermore, the radius of the circle in the VPDs is larger for saturated and very-faint stars to take into account for their larger relative PM errors.

Finally, Fig. 3 presents the m_{F606W} versus $(m_{F606W} - K_S)$ CMD for stars members of HP 1 according to their relative PMs.

3.1 Non-linear effects in GSAOI photometry

As previously reported by Massari et al. (2016a) and Saracino et al. (2016), GSAOI + GeMS photometry presents non-linearity effects. These issues mainly affect RGB stars, steepening the slope of the RGB.

We adopted an a-posteriori, empirical correction to mitigate the non-linearity effects. We compared the K_S photometry of the stars in the long exposures with that obtained from the short exposures zero-pointed to the long-exposure photometric system. For stars at the MSTO, for which we do not expect non-linearity effects, we found an agreement between the long- and the short-based magnitudes. In the magnitude interval within which the linearity effects become sizeable in the long but not in the short exposures ($13 < K_S < 15$), we measured stars systematically fainter in the long than in the short exposures. For brighter magnitudes, the non-linearity effects and saturation problems are also present in the short exposures, thus limiting any further investigation. As such, we adopted only stars with $13 < K_S < 15$ to compute our correction.

We found that a straight line is enough to model the non-linearity effects in the magnitude range $13 < K_S < 15$ (Fig. 4). The correction to add to the GSAOI K_S magnitudes brighter than $K_S < 15$ was extrapolated by this straight line. We do not have J-filter short exposures; therefore, we corrected the J photometry using the same linear relation as for the K_S magnitudes.

The original (left-hand panel) and non-linearity-corrected (right-hand panel) CMDs are shown in Fig. 5. We drew a fiducial line of the RGB stars using the original (red line) and the corrected (blue line) photometry to highlight the difference in the RGB slope before and after the correction. The correction is fairly good up to $K_S \sim 13$, while for brighter stars it is underestimated. Although this correction is enough for a more reliable isochrone fit, the correction is applied only to improve the cosmetics of the CMDs. In the following sections, we limited our analysis to stars fainter than $K_S = 15$. Hereafter, we used only the corrected photometry in our CMDs unless explicitly declared otherwise.

4 STELLAR EVOLUTIONARY MODELS

To compare our GSAOI and *HST* data with theoretical stellar evolutionary models, we employed two sets of isochrones:

(i) *Dartmouth Stellar Evolutionary Database* (DSED; Dotter et al. 2008)[4] and

(ii) *A Bag of Stellar Tracks and Isochrones* (BaSTI Pietrinferni et al. 2006).[5]

In both cases, we retrieved α-enhanced ([α/Fe] = + 0.40) isochrones with canonical helium ($Y \sim 0.25$), metallicities similar to the one from HP 1 ([Fe/H] ~ -1.0), and covering ages from

[4] http://stellar.dartmouth.edu/models/
[5] http://albione.oa-teramo.inaf.it

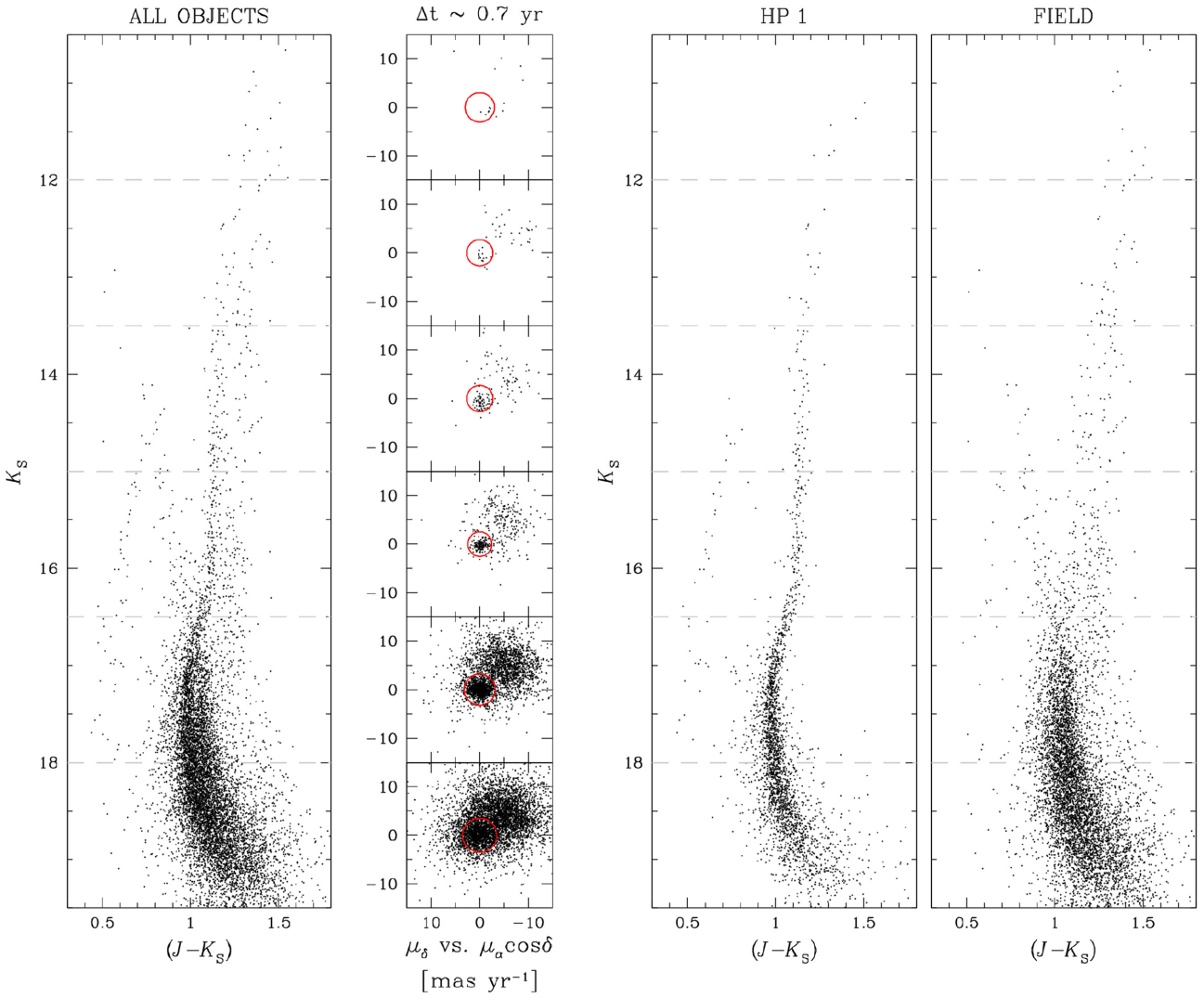

Figure 2. In the left-hand panel, we present the K_S versus $(J - K_S)$ CMD of all stars in the FoV. Only well-measured (both astrometrically and photometrically) stars are shown. We divided our sample in six 1.5-magnitude bins to better infer the cluster membership. The grey, dashed horizontal lines are the limits of each magnitude bin. In the middle-left VPDs, the red circles are centred at (0,0) mas yr^{-1} and have a radius of 3.0, 2.7, 2.7, 2.5, 3.2, 3.5 mas yr^{-1} from top to bottom, respectively. Stars within these circles are considered as likely members of HP 1. The CMD of the cluster members is presented in the middle-right panel. In the CMD on the right, we plot only field stars. The separation between HP 1 and field objects is not clear, especially at faint magnitudes, and might result in a contamination of sources members of one population into the sample of the other.

10.0 to 15.0 Gyr in steps of 0.20 Gyr. DSED and BaSTI isochrones are available in the ACS/WFC@*HST* photometric system, but only the former were converted to the 2MASS photometric system by the original developers. On the other hand, BaSTI NIR colours are originally in the Johnson–Cousins–Glass photometric system, so they were first converted to the Bessel & Brett (1988) system and then to the 2MASS photometric system using the transformations presented in the final 2MASS data release.[6]

Fig. 6 illustrates the DSED and BaSTI isochrones used in this work, showing the effect of the age and metallicity in the M_{K_S} versus $M_J - M_{K_S}$ and M_{F606W} versus $(M_{F606W} - M_{K_S})$ CMDs. Interpolations in metallicity were performed in order to compute isochrones with $-1.26 \leq$ [Fe/H] ≤ -0.86 in steps of 0.02 dex, therefore fully covering the accurate value of [Fe/H] $= -1.06 \pm 0.10$ from high-resolution spectroscopic analysis of Barbuy et al. (2016).

[6] http://www.astro.caltech.edu/ jmc/2mass/v3/transformations

Although the DSED and BaSTI models seem to produce isochrones that are almost indistinguishable, they present slightly distinct age scales. Differently from the DSED code, the effects of atomic diffusion were not incorporated in the BaSTI one. This leads to an apparent overestimation in the ages from the BaSTI models of about 0.9 Gyr in relation to the models where the atomic diffusion is included (Cassisi et al. 1998, 1999, and references therein). In Section 6, we address this issue in order to find not only the systematic differences in age between the BaSTI and DSED but also those in the other parameters.

5 CONSTRAINTS FROM COLOUR–COLOUR DIAGRAMS AND RR LYRAE STARS

Taking the advantage of deep multiband photometry, from optical (F606W) to NIR (J and K_S), as well as the presence of RR Lyrae stars towards the cluster that were identified by the OGLE Collection of

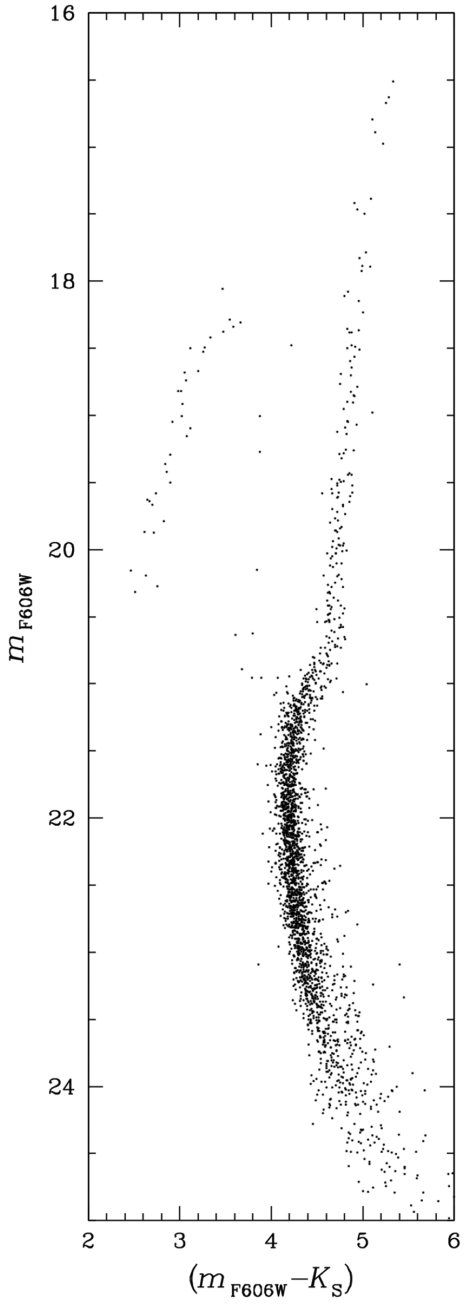

Figure 3. m_{F606W} versus $(m_{F606W} - K_S)$ CMD of likely members of HP 1.

Variable Stars (Soszyński et al. 2014), we obtained some constraints on the reddening and distance values of HP 1.

Due to the limitation in the photometric depth, the previous simultaneous determinations of these parameters were based on red giant stars. Using a V versus $V - I$ CMD obtained with NTT data, Ortolani, Bica & Barbuy (1997) recovered colour excess $E(B - V) = 1.19$ and a distance $d_\odot = 6.75 \pm 0.60$ kpc [or an intrinsic distance modulus of $(m - M)_0 = 14.15 \pm 0.20$]. These authors found an RGB slope similar to the one of NGC 6752 ([Fe/H] ~ -1.5). From the analysis of a K versus $(J - K)$ CMD built with NIR images collected with the same telescope, Valenti et al. (2010) determined very similar reddening [$E(B - V) = 1.19$] and distance modulus [$(m - M)_0 = 14.17$, equivalent to $d_\odot = 6.8$ kpc], but a slightly less metal-poor solution ([Fe/H] $= -1.12$), in very good

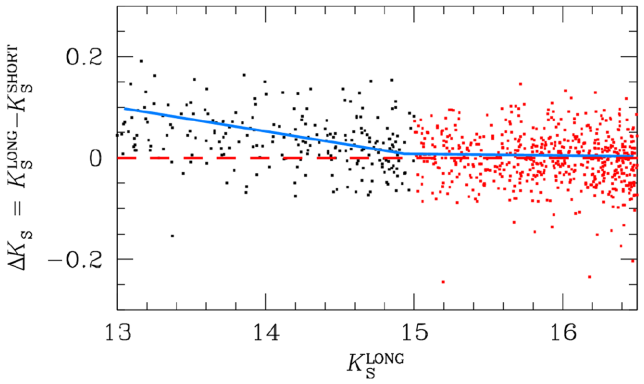

Figure 4. Difference between long- and short-exposure K_S magnitudes. Red points refer to stars for which the non-linearity effects are negligible in both long and short exposures, while black points mark objects for which the effects are sizeable only in the long exposures. The blue line represents the linear relation made by hand to interpolate (and correct) the non-linearity in the GSAOI@Gemini-S photometry.

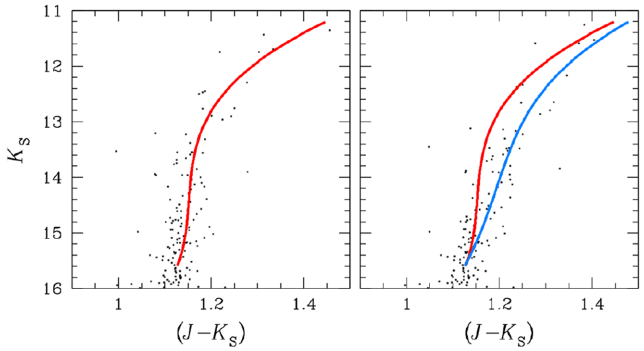

Figure 5. Difference between the original (left) and non-linearity-corrected (right) K_S versus $(J - K_S)$ CMDs of HP 1. The red and the blue lines represent the HP 1 RGB fiducial lines in the original and corrected photometry, respectively.

agreement with the recent spectroscopic result from Barbuy et al. (2016) ([Fe/H] $= -1.06 \pm 0.10$).

Finally, Ortolani et al. (2011) built a PM-cleaned CMD using their previous NTT images in the V filter as the first-epoch and MAD@VLT images in the J and K_S filters as the second one. By means of an isochrone fit using Padova models with [Fe/H] ~ -1.0, they determined a colour excess $E(V - K_S) = 3.3$ ($\sim E(B - V) = 1.17$) and a distance of $d = 7.1 \pm 0.5$ kpc, in both cases assuming a $R_V = A_V/E(B - V) = 3.2$. They also recovered a short distance of 6.8 kpc comparing the magnitude difference in V between the HP 1 HB stars at the RR Lyrae level and that of the bulge field. In this case, they assumed as the solar distance to the Galactic Centre a value of 8.0 kpc.

5.1 Colour–colour diagram and reddening

Colour–colour diagrams are useful tools to determine the reddening of a cluster, since they do not depend on the distance. Despite this fact, they should be used with caution since colours – in particular involving optical and NIR – might present systematic uncertainties caused by small zero-point corrections in the photometric calibrations. Furthermore, when $E(B - V) \gtrsim 0.3$ (or $A_V \gtrsim 1.0$), as in the present case, the reddening and extinction dependence on

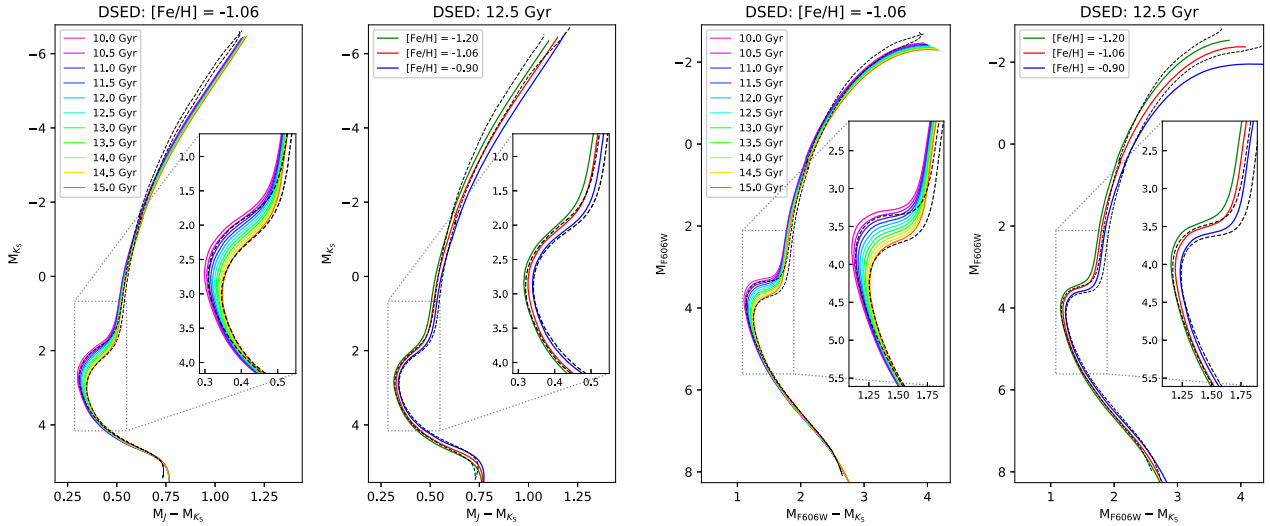

Figure 6. Isochrones from DSED models showing the effect of age (10.0–15.0 Gyr, for a metallicity [Fe/H] = −1.06) and metallicity ([Fe/H] = −1.20, −1.06, −0.90, for an age of 12.5 Gyr) in the M_{K_S} versus $M_J - M_{K_S}$ CMD (left-hand panels) and in the M_{F606W} versus ($M_{F606W} - M_{K_S}$) (right panels) CMD. All models have [α/Fe]=+0.40 and canonical helium abundance ($Y \sim 0.25$). BaSTI isochrones with the extreme age and [Fe/H] values are also presented (dashed lines).

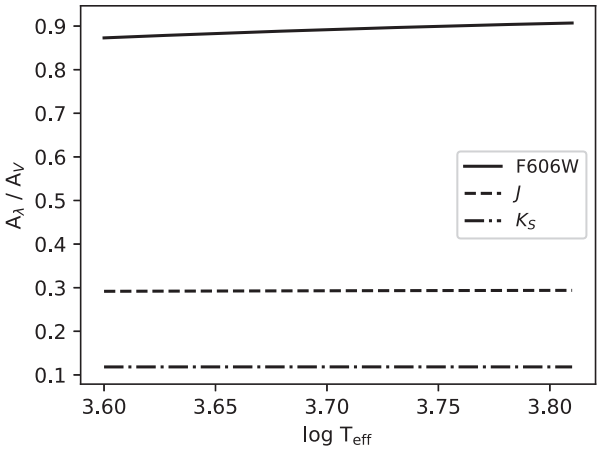

Figure 7. A_{F606W}/A_V (solid line), A_J/A_V (dashed line), A_{K_S}/A_V (dotted-dashed line) as a function of the star effective temperature.

the effective temperature (T_{eff}) become relevant, particularly in the visible range. It means that in this high reddening regime a single value for ratios between the extinction in a given photometric band (A_λ) and A_V is no longer a good approximation, particularly to analyse very accurate photometry in the optical. Furthermore, it is important to point out that R_V depends on the colour and on the reddening value (McCall 2004). For our typical CMD colours and extinction, $R_V = 3.2$ appear more suitable than the standard value of 3.1.

To compute A_λ/A_V as a function of $\log T_{eff}$, we used the CMD 3.0 web interface,[7] which implemented the results from Girardi et al. (2008) models, to retrieve PARSEC isochrones (Bressan et al. 2012) with $E(B-V) = 0.00$ and $E(B-V) = 1.15$. Therefore, the desired relations are obtained by measuring the magnitude differences between these isochrones as a function of $\log T_{eff}$ (Fig. 7). As

[7] http://stev.oapd.inaf.it/cgi-bin/cmd

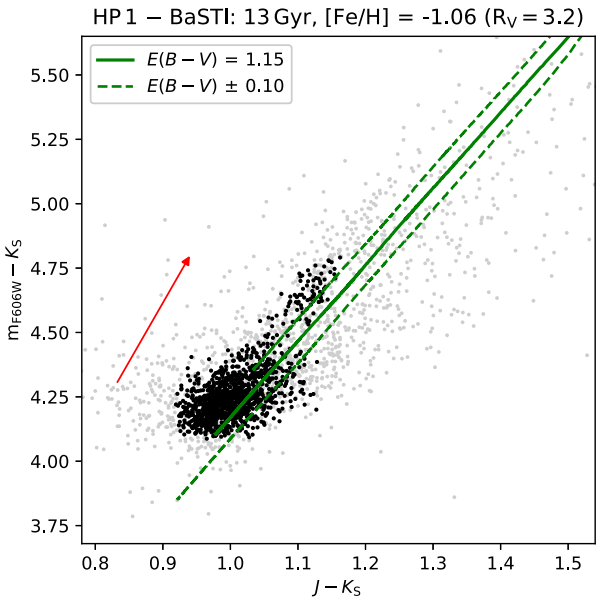

Figure 8. Colour–colour diagram of HP 1. The green solid line corresponds to a BaSTI isochrone with age of 13.0 Gyr, [Fe/H] = −1.06, $R_V = \frac{A_V}{E(B-V)} = 3.2$, and $E(B-V) = 1.15$. An uncertainty of 0.10 in $E(B-V)$ is limited by the green dashed lines. The red arrow corresponds to a reddening vector of $E(B-V) = 0.20$. Black points correspond to the ones used in the isochrone fits (see Section 6).

expected, the A_λ/A_V variation is only significant in the F606W filter (∼5 per cent), whereas it is almost negligible in the NIR filters.

Fig. 8 presents the colour–colour ($m_{F606W} - K_S$) versus ($J - K_S$) diagram for HP 1. An α-enhanced ([α/Fe]=+0.40]) BaSTI isochrone with [Fe/H] = −1.06 and 13.0 Gyr was chosen as a reference for the colours. A reddening value of $E(B-V) = 1.15 \pm 0.10$ generates a good overall fit, in accordance with previous determinations from literature. This range in reddening was used by us to estimate the distances of the RR Lyrae, whereas a wide

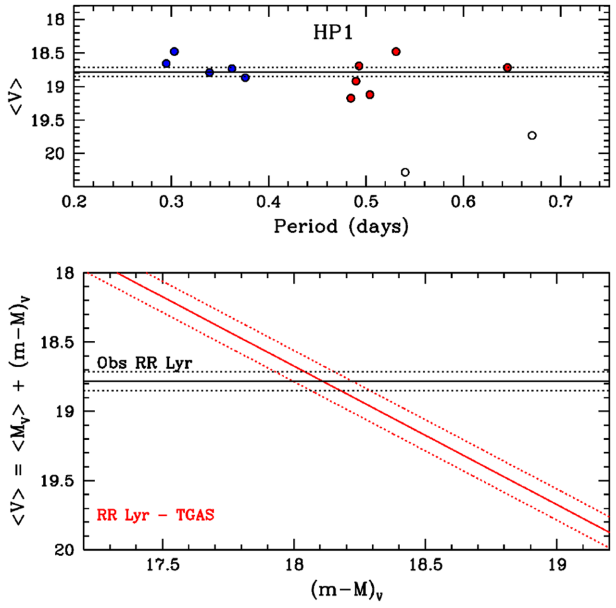

Figure 9. Mean V magnitudes versus period of the RRab (red circles) and RRc (blue circles) Lyrae stars in HP 1 (top panel) and the expected apparent distance modulus in V for these stars assuming an $M_V = 0.67 \pm 0.11$ (red lines) (bottom panel). All RR Lyrae stars come from the OGLE CVS. The absolute magnitude in V was determined using [Fe/H] $= -1.06 \pm 0.10$ and the empirical M_V–[Fe/H] relations from the Gaia Collaboration (2017) using the TGAS. The mean of the mean V magnitudes (solid black line) and its standard deviation (dotted lines) is shown in both panels. Two rejected RR Lyrae stars are also presented (open circles).

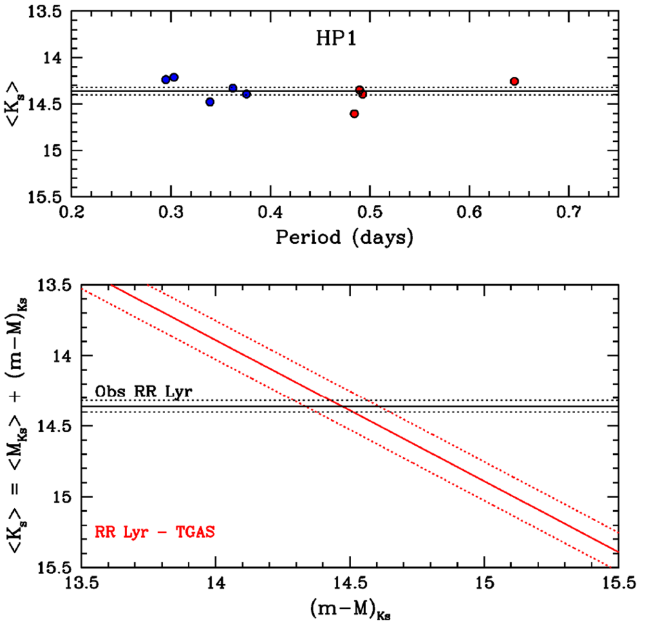

Figure 10. Same as Fig. 9, but for the K_S filter. In this case, we adopted $M_{K_S} = -0.11 \pm 0.14$ from the $PM_{K_S}Z$ relations from Gaia Collaboration (2017). The K_S magnitudes come from the VVV survey.

range of $\Delta E(B-V) = 0.360$ was employed to impose initial limits in the isochrone fits (see Section 6).

5.2 RR Lyrae and distances

RR Lyrae stars are Population II pulsating stars and one of the fundamental primary distance indicators in astronomy. Presenting periods under a day and light-curve amplitudes from few tenths of magnitude in K_S to ∼1 mag in V, these core helium burning stars are very common in old GCs with [Fe/H] $\lesssim -1.0$ since these systems present HB stars populating the instability strip. Therefore, RR Lyrae stars are ideal standard candles to impose independent constraints on distance in a moderately metal-poor bulge GC-like HP 1. Using the OGLE CVS for the Galactic bulge (Soszyński et al. 2014), we identified 13 RR Lyrae stars within 150 arcsec from the cluster centre. The mean V magnitude and periods for these stars are presented in Fig. 9 (upper panel), where it is possible to identify two probable foreground field stars. The remaining 11 RR Lyrae stars are divided in 6 of RRab type and 5 of RRc type, providing a value of 18.78 ± 0.07 for the mean of the mean V magnitudes ($\langle V \rangle$).

In order to determine the apparent distance modulus for these stars, one needs a prediction for the absolute V magnitude (M_V) for the HP 1 metallicity ([Fe/H] $= -1.06 \pm 0.10$). For this purpose, we used the very recent empirical calibrations for the M_V –[Fe/H] relation from the Gaia Collaboration (2017) based on *Tycho–Gaia* Astrometric Solution (TGAS). Taking into account the uncertainties in the HP 1 metallicity, the systematics and stochastic effects from the three different methods to perform such calibration, we obtained an average value of $\langle M_V \rangle = 0.67 \pm 0.11$. Since, by definition, the apparent distance modulus in V is the difference between V and M_V, the $(m-M)_V$ value for HP 1 is 18.11 ± 0.18. This result is illustrated in Fig. 9 (bottom panel) by the intersection between the observed $\langle V \rangle$ value (black line) and the one expected for RR Lyrae stars assuming the TGAS calibration [red line; $\langle V \rangle = \langle M_V \rangle + (m - M)_V$]. Assuming an $R_V = 3.2 \pm 0.10$ and a conservative value of $E(B-V) = 1.15 \pm 0.10$, we derive a value of $A_V = 3.68 \pm 0.34$ for the extinction in V. This result leads us to an intrinsic distance modulus of $(m-M)_0 = 14.43 \pm 0.38$, which means a large and high uncertain heliocentric distance of $7.7^{+1.5}_{-1.2}$ kpc.

A more reliable and accurate result for the apparent distance modulus and distance from RR Lyrae stars can be reached using the K_S filter. This is a natural and straightforward consequence of a significantly lower extinction in K_S than in V ($A_{K_S}/A_V = 0.1185$), as well as period–luminosity relationships with very low scattering (e.g. Beaton et al. 2016). To take advantage of the NIR photometry, we performed a cross-match between the RR Lyrae stars from the OGLE CVS with the stars presented in the *VISTA Variables in the Via Lactea* (VVV) survey (Saito et al. 2012).[8]

Fig. 10 (upper panel) presents the results for the nine RR Lyrae stars recovered in this process, where a threshold of 1.0 arcsec in the source separation was applied. The mean of the mean K_S magnitude of these stars is 14.36 ± 0.04. Using the mean solution of the three empirical M_{K_S}–log P–[Fe/H] relations ($PM_{K_S}Z$) from the Gaia Collaboration (2017), we estimated an average absolute K_S magnitude for the HP 1 RR Lyrae stars of −0.11 ± 0.14. Random and systematic uncertainties in these calibrations were taken into account. A metallicity of [Fe/H] $= -1.06 \pm 0.10$ and a mean period of 0.42 ± 0.04 d were considered to compute this value. Therefore, the expected apparent distance modulus in K_S of HP 1 is 14.47 ± 0.18, as shown in Fig. 10 (bottom panel). Subtracting from this value the expected A_{K_S} ($0.1184 \times A_V = 0.44 \pm 0.04$, assuming once again $E(B-V) = 1.15 \pm 0.10$ and $R_V = 3.2 \pm$

[8] https://vvvsurvey.org

0.10), an intrinsic distance modulus of $(m - M)_0 = 14.03 \pm 0.18$ is recovered. Converted to the heliocentric distance, this value means $6.4^{+0.6}_{-0.5}$ kpc. It is interesting to note that this result is independent of the uncertainty in the R_V value, and is almost unaffected by those in reddening.

Although the two distance determinations presented in this section agree within the errors, a shorter distance scale is clearly favoured because the result obtained with the NIR photometry present uncertainties that are significantly smaller than those obtained from the *V*-filter analysis. Furthermore, a value of $6.4^{+0.6}_{-0.5}$ kpc is in good agreement with the previous determinations from NIR (Valenti et al. 2010; Ortolani et al. 2011) and optical (Ortolani et al. 1997).

5.3 RR Lyrae stars and He content

RR Lyrae stars are core helium burning stars, thus an increase in luminosity is expected for those that are He-enhanced objects. Therefore, they can provide a good constraint to the He abundance, which in turn can help one to derive more reliable ages.

A simple comparison between BaSTI models for HB stars with $Y \sim 0.25$ and $Y = 0.30$ indicates that a helium enhancement of $\Delta Y \sim 0.05$ (for [Fe/H] ~ -1.0) produces RR Lyrae stars that are ∼0.20 mag brighter in *V*. It means an increase of the same amount in terms of $(m - M)_V$ or $(m - M)_0$, towards more discrepant values, producing an unreliable heliocentric distance of 8.4 kpc for HP 1.

Very recently Lagioia et al. (2018) and Milone et al. (2018) found that the differences in He content between first and second stellar generations are small, amounting to $\Delta Y \lesssim 0.03$. As demonstrated by Nardiello et al. (2015), such He-enhancement, if present, would be related to age differences of ≲300 Myr, even taking into account [Fe/H] and [α/Fe] variations of 0.02 dex between the stellar generations.

6 ISOCHRONE FITTING

6.1 Our method

To derive ages, metallicity, intrinsic distance moduli [$(m - M)_0$], and reddening values [$E(B - V)$] in an objective and self-consistent way, we performed isochrone fits using a Bayesian approach. For simplicity reasons, we assume that HP 1 can be considered as a single stellar population (SSP), which is a very reliable hypothesis given its relatively low mass. Besides there is no information in this respect, since this clusters has not been observed in ultraviolet filters cf. Piotto et al. (2015). Similar methods have been successfully tested and applied to analyse CMDs of open clusters (Naylor & Jeffries 2006; Monteiro, Dias & Caetano 2010; Alves et al. 2012), Galactic GC (Hernandez & Valls-Gabaud 2008; Wagner-Kaiser, Sarajedini & von Hippel 2017; Kerber et al. 2018), and stellar clusters in the Magellanic Clouds (Dias et al. 2016b; Pieres et al. 2016; Perren, Piatti & Vázquez 2017). In brief, by computing the likelihood statistics, our method determines the isochrones that best reproduce the observed CMD. First, for the *j*th isochrone displaced by a given intrinsic distance modulus and reddening vector, we compute the minimum distance of the *i*th observed star to it, defined as

$$r_{ij} = \min \left[\left(\frac{\text{colour}_i - \text{colour}_j}{\sigma_{\text{colour},i}} \right)^2 + \left(\frac{\text{mag}_i - \text{mag}_j}{\sigma_{\text{mag},i}} \right)^2 \right]^{1/2}, \quad (1)$$

where $\sigma_{\text{colour},i}$ and $\sigma_{\text{mag},i}$ are the uncertainties in colour and magnitude of this observed star. Then, the probability of the *i*th observed star to belong to the *j*th isochrone is given by

$$p_{ij} \propto \frac{1}{\sigma_{\text{colour},i}\, \sigma_{\text{mag},i}} \exp\left(\frac{-r_{ij}^2}{2} \right). \quad (2)$$

Finally, the logarithmic likelihood that the total observed stars (N_{obs}) are drawn from the *j*th isochrone can be written by

$$\ln \mathcal{L} = \ln \sum_{i=1}^{N_{\text{obs}}} p_{ij} \propto -2 \sum_{i=1}^{N_{\text{obs}}} r_{ij} - \sum_{i=1}^{N_{\text{obs}}} \ln(\sigma_{\text{colour},j}) - \sum_{i=1}^{N_{\text{obs}}} \ln(\sigma_{\text{mag},j}). \quad (3)$$

To test all acceptable solutions, we explore a wide and regular grid in the all parameter space, where the centre corresponds to the values used in our control experiments (see Section 6.2). The grid we employed typically covers ΔAge = 5.0 Gyr, $\Delta E(B - V) = 0.360$, $\Delta(m - M)_0 = 0.90$, and Δ[Fe/H] = 0.40 dex in steps of 0.2 Gyr, 0.008 mag, 0.02 mag, and 0.02 dex, respectively. We applied the Markov chain Monte Carlo (MCMC) sampling technique to obtain the final parameters, as well as to study the confidence intervals and correlations between them. For this purpose, we used the `emcee` code (Foreman-Mackey et al. 2013) to sample the posterior probability in the four-dimensional parameter space, assuming a uniform prior probability distribution within the acceptable physical ranges.

The final solutions correspond to the sum of the posterior probability distributions over 10 MCMC samples in order to minimize the stochastic effects of the Monte Carlo methods. The uncertainties in each parameter depend on several factors, such as the photometric errors, the photometric depth, the contamination by field stars, the filters choice, and even the quality of the stellar evolutionary models. As can be seen by the sanity checks discussed in the next section and the results presented in Section 7, in this work the typical formal uncertainties from the MCMC for age, [Fe/H], $(m - M)_0$, and $E(B - V)$ are ∼ 0.6 Gyr, 0.07 dex, 0.04 mag, and 0.03 mag, respectively. To improve the quality of the fit, we restrict our analysis to the stars within 3.0σ from the median colour position for each magnitude bin, therefore minimizing the influence of the remaining field stars and other outliers that are not predicted by the isochrones (e.g. blue stragglers, and binaries). All the details of the PYTHON code developed by us to make the isochrone fitting will be presented in a future paper (Souza et al., in preparation).

6.2 Control experiments

To validate our isochrone fitting technique, we performed some control experiments with synthetic CMDs. Artificial photometric catalogues mimicking the HP 1 data were generated, providing synthetic data with known input parameters. This was done using a DSED isochrone with 12.5 Gyr, [Fe/H] = −1.06, $E(B - V) = 1.15$, and $(m - M)_0 = 14.05$. A number of artificial stars similar to HP 1 were randomly drawn assuming the observed photometric uncertainties and educated guesses for the binary fraction (30 per cent) and for the Initial Mass Function (Salpeter). The results for a simple sanity check in the K_S versus $(J - K_S)$ CMD are presented in Fig. 11, where it is possible to attest that our method is recovering the expected parameters within the uncertainties. Similar successful results are also obtained for sanity checks in the optical-NIR CMD, as well as using BaSTI isochrones.

As discussed in Section 4, it is expected that ages recovered using BaSTI isochrones will be older than the ones from fits with

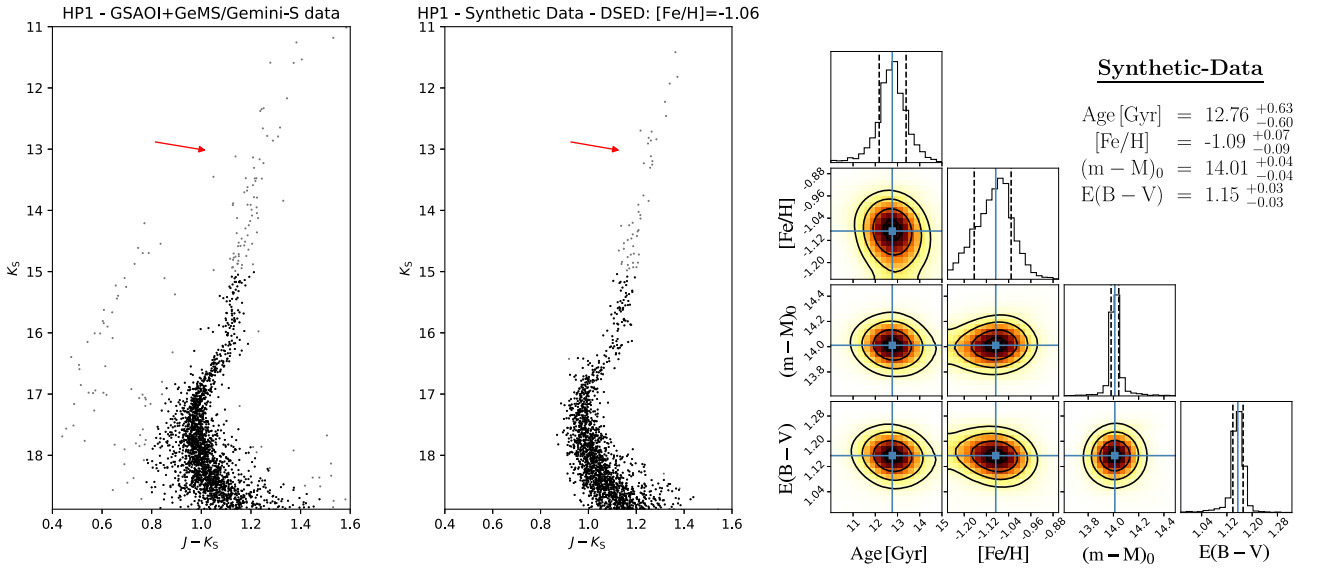

Figure 11. Results of a sanity check for our isochrone fitting technique in the K_S versus $(J - K_S)$ CMD. Left-hand panel: HP 1 data. Middle panel: synthetic CMD of HP 1 generated with DSED models. The input parameters are 12.5 Gyr, [Fe/H] $= -1.06$, $E(B - V) = 1.15$, and $(m - M)_0 = 14.05$. Only stars within 3.0σ from the median colour position (black points) are used in the fit. Right-hand panels: corner plots showing the output of the MCMC method and the recovered physical parameters. These panels present the one- and two-dimensional projections of the posterior probability distribution for all parameters. The contours correspond to the $[0.5\sigma, 1.0\sigma, 1.5\sigma, 2.0\sigma]$ levels.

DSED isochrones. To quantify this effect and possible trends in the other parameters according to the choice in the stellar evolutionary models, we computed two additional control experiments. Once again, a DSED isochrone with 12.5 Gyr, [Fe/H] $= -1.06$, $E(B - V) = 1.15$, and $(m - M)_0 = 14.05$ was used as the input. It is a convenient choice since the treatment for atomic diffusion is only present in the DSED code. To avoid unnecessary stochastic effects, only the original isochrone magnitudes and colours were employed. By comparing this DSED isochrone with a regular and wide grid in the parameters space using BaSTI isochrones, we were able to determine the expected differences in the physical parameters. Note that in these tests we forced the metallicity to be fixed at -1.06. Fig. 12 reveals that our isochrone fits using BaSTI models recover solutions that are on average $\sim$0.9 Gyr older, $\sim$0.02 less red, and $\sim$0.05 closer (in intrinsic distance modulus) than the ones with DSED models. In Section 7, we will apply the opposite of these offsets in order to correct the BaSTI solutions for atomic diffusion (hereafter, BaSTI*), therefore generating final values for the physical parameters that can be better compared.

7 RESULTS FROM ISOCHRONE FITTING

7.1 The K_S versus $(J - K_S)$ CMD

Figs 13 and 14 present the best isochrone fits in the K_s versus $J - K_s$ CMD, using DSED and BaSTI models. In each of these figures, we present an overview of the best solution with zoom showing the stars that were effectively used during the fit (left-hand panel) and the output of the MCMC method (right-hand panels). The best fits provide excellent solutions for both stellar evolutionary models, as attested by the overplotted isochrone and by the well-defined posterior probability distributions in the corner plots. The recovered physical parameters for all fits using the NIR CMD are presented in the upper part of Table 1. According to the analysis using DSED models, the age of HP 1 from this CMD is $13.0^{+0.9}_{-0.6}$ Gyr, with an intrinsic distance modulus of 14.06 ± 0.05, which means a distance of $6.49^{+0.15}_{-0.15}$ kpc, a reddening value of $E(B - V) = 1.13 \pm 0.03$ and a metallicity of [Fe/H] $= -1.07^{+0.07}_{-0.10}$. It is important to highlight that only assume a uniform prior probability distribution for metallicity during the isochrone-fitting process, and even so the recovered value is in very good agreement with the one estimated with high-resolution spectroscopy (Barbuy et al. 2016).

A very interesting consistent check can be done by comparing the apparent distance modulus from the isochrone fits with those from the RR Lyrae stars. The DSED models predict a value of 14.49 ± 0.05 for the apparent distance modulus in K_S, in perfect agreement with the one determined in Section 5.2 (see Fig. 10). It is important to note that these two results are totally independent and based on pure NIR data, reinforcing a short-scale distance for HP 1.

The original results with BaSTI models point to a very old age of $13.8^{+0.9}_{-1.2}$ Gyr, being in the limit of the age of the Universe (13.799 ± 0.021 Gyr; Planck Collaboration XIII 2016). This age is reduced to $12.9^{+0.9}_{-1.2}$ Gyr after the expected correction of 0.9 Gyr due to the atomic diffusion, putting the new value in very good agreement with the one from DSED. Furthermore, the expected offsets for the other parameters leave the distance and reddening from BaSTI and DSED in a perfect match.

7.2 The m_{F606W} versus $(m_{F606W} - K_S)$ CMD

The best isochrone fits using the m_{F606W} versus $(m_{F606W} - K_s)$ CMD and DSED and BaSTI models are presented in Figs 15 and 16. The recovered physical parameters for all fits using the optical-NIR CMD are presented in the bottom part of Table 1. As in the pure NIR data, the best solutions reproduce the CMD features very well. The corner plots from the MCMC method present well-defined one- and two-dimensional projections of the posterior probability

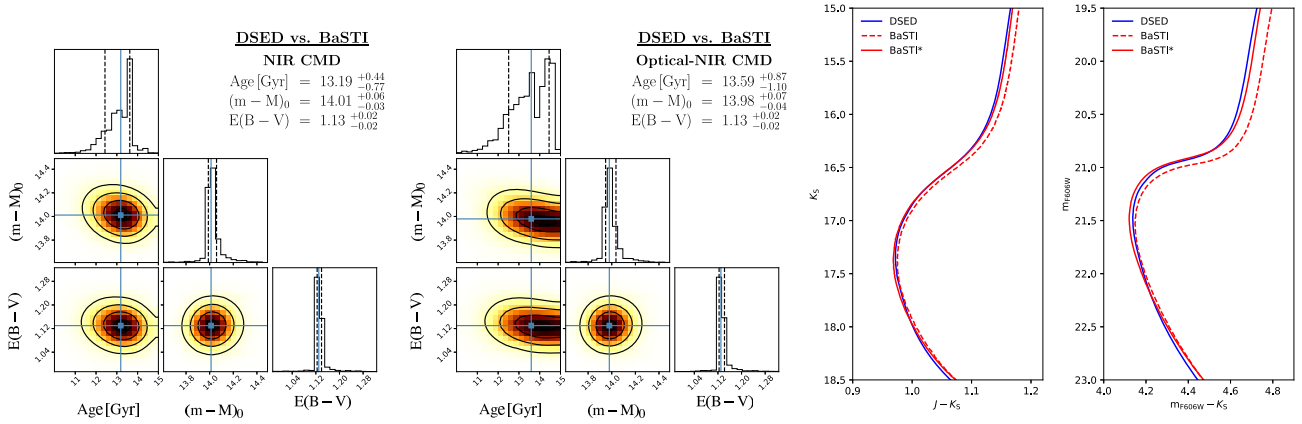

Figure 12. Results for two control experiments to quantify the expected differences in the physical parameters according with the stellar evolutionary choice. An DSED isochrone with 12.5 Gyr, [Fe/H] $= -1.06$, $E(B-V) = 1.15$, and $(m-M)_0 = 14.05$ was used as input and compared with a regular grid of BaSTI isochrones. Left-hand panels: Corner plots showing the output of the MCMC method for the K_S versus $(J-K_S)$ CMD. Middle panels: Results for the m_{F606W} versus $(m_{F606W}-K_S)$ CMD. They present the one- and two-dimensional projections of the posterior probability distribution for all parameters. The contours correspond to the $[0.5\sigma, 1.0\sigma, 1.5\sigma, 2.0\sigma]$ levels. Right-hand panels: The DSED isochrone used as input (blue solid line) and a BaSTI isochrone with the same parameters (red dashed line). We also present a BaSTI isochrone 1.0 Gyr younger and displaced by $\Delta E(B-V) = 0.02$ and $\Delta(m-M)_0 = 0.05$ (BaSTI*).

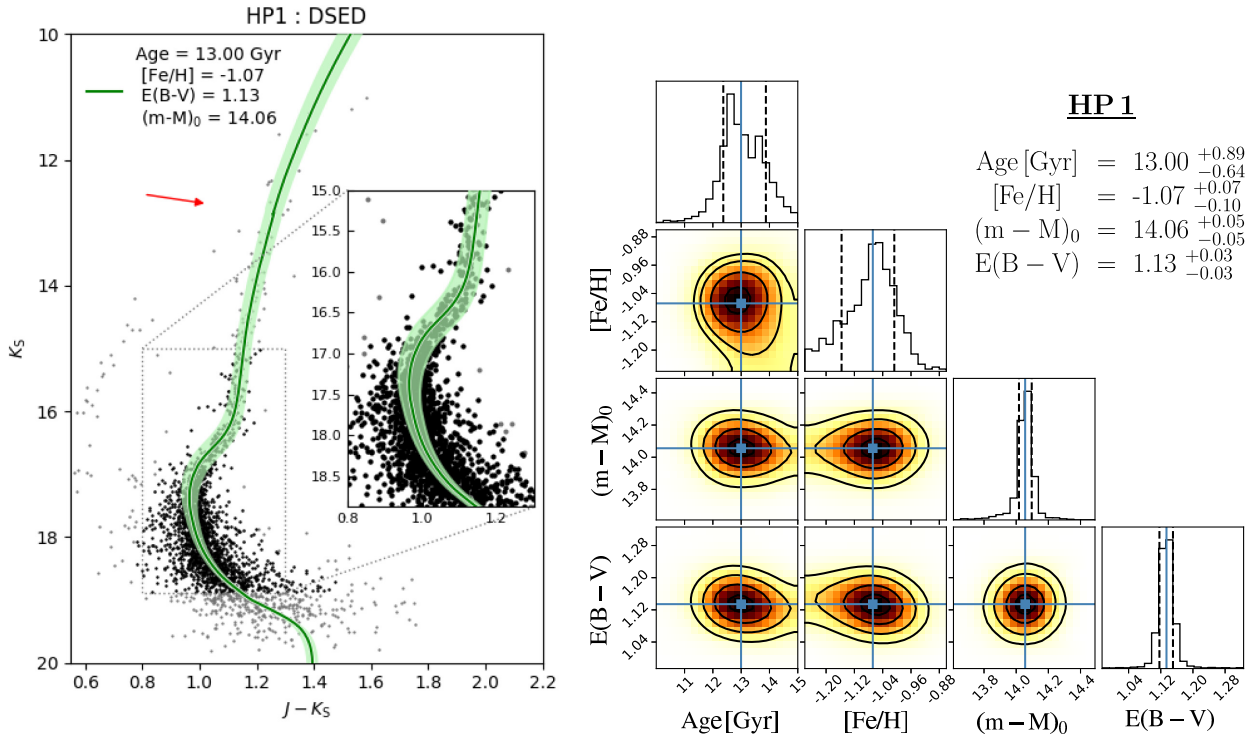

Figure 13. Best isochrone fit in the K_s versus $(J-K_s)$ CMD using DSED models. Left-hand panel: CMD showing all observed stars (grey) and those used in the fit (black). A reddening vector corresponding to $\delta E(B-V) = 0.10$ is also presented, and a zoom in the CMD region that is more sensitive to the age. The best fit is highlighted by a thick line. The green area shows the region between the two isochrones using the values within 1.0σ for all the parameters. Right-hand panels: Corner plots showing the output of the MCMC method. They present the one- and two-dimensional projections of the posterior probability distribution for all parameters. The contours correspond to the $[0.5\sigma, 1.0\sigma, 1.5\sigma, 2.0\sigma]$ levels.

distributions for all parameters (Foreman-Mackey 2016), attesting the high quality of the fits.

The results from DSED isochrones in this optical-NIR CMD indicate an age of $12.71^{+0.70}_{-0.54}$ Gyr, in excellent agreement with the one presented for in the previous subsection. Although a slightly higher intrinsic distance modulus (or distance) is recovered here, this value agrees within 1σ with the one from the analysis of GSAOI+GeMS data. The same cannot be said for the reddening: it is clearly higher when the optical *HST* data is introduced in the analysis. With respect to the metallicity, the recovered value is in good agreement both in the fitting with the NIR data and with the spectroscopic analysis.

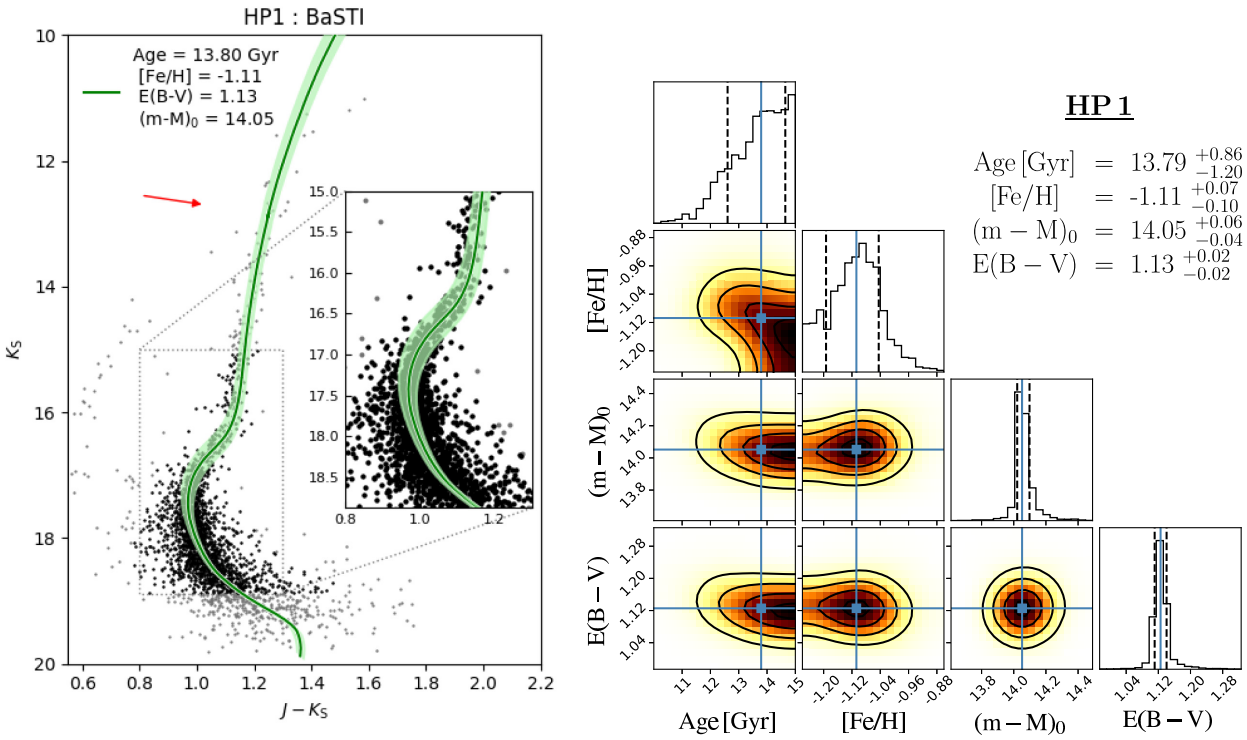

Figure 14. Same as Fig. 13, but for BaSTI models.

Table 1. Physical parameters for HP 1 from isochrone fits using α-enhanced ([α/Fe] = + 0.40) BaSTI and DSED models in the K_S versus $(J - K_S)$ and m_{F606W} versus $(m_{F606W} - K_S)$ CMDs.

Model	[Fe/H]	Age (Gyr)	$(m - M)_0$	$d_\odot$ (kpc)	$E(B - V)$	$(m - M)^a$
			K_S versus $(J - K_S)$ CMD			
DSED	$-1.07^{+0.07}_{-0.10}$	$13.00^{+0.89}_{-0.64}$	$14.06^{+0.05}_{-0.05}$	$6.49^{+0.15}_{-0.15}$	$1.13^{+0.03}_{-0.03}$	$14.49^{+0.05}_{-0.05}$
BaSTI	$-1.11^{+0.07}_{-0.10}$	$13.79^{+0.86}_{-1.20}$	$14.05^{+0.06}_{-0.04}$	$6.46^{+0.18}_{-0.12}$	$1.13^{+0.02}_{-0.02}$	$14.48^{+0.0}_{-0.0}$
BaSTI*[b]	$-1.11^{+0.07}_{-0.10}$	$12.89^{+0.86}_{-1.20}$	$14.10^{+0.06}_{-0.04}$	$6.61^{+0.19}_{-0.12}$	$1.15^{+0.02}_{-0.02}$	$14.54^{+0.06}_{-0.04}$
			m_{F606W} versus $(m_{F606W} - K_S)$ CMD			
DSED	$-1.06^{+0.05}_{-0.06}$	$12.71^{+0.70}_{-0.54}$	$14.09^{+0.05}_{-0.06}$	$6.58^{+0.15}_{-0.18}$	$1.16^{+0.02}_{-0.02}$	$17.80^{+0.08}_{-0.09}$
BaSTI	$-1.12^{+0.08}_{0.08}$	$13.31^{+0.99}_{-0.86}$	$14.08^{+0.06}_{-0.05}$	$6.55^{+0.18}_{-0.15}$	$1.15^{+0.02}_{-0.02}$	$17.76^{+0.09}_{-0.08}$
BaSTI*[b]	$-1.12^{+0.08}_{+0.08}$	$12.41^{+0.99}_{-0.86}$	$14.13^{+0.06}_{-0.05}$	$6.70^{+0.19}_{-0.16}$	$1.17^{+0.02}_{-0.02}$	$17.87^{+0.09}_{-0.08}$
			Average results (DSED & BaSTI*[b] models)			
	$-1.09^{+0.07}_{-0.09}$	$12.75^{+0.86}_{-0.81}$	$14.10^{+0.06}_{-0.05}$	$6.59^{+0.17}_{-0.15}$	$1.15^{+0.02}_{-0.02}$	–

Notes. [a] $(m - M)$ is the apparent distance modulus in the K_s filter (for the NIR CMD) or in the V filter (for the optical-NIR CMD).
[b] BaSTI* is the BaSTI results after the expected correction for atomic diffusion (see Sections 4 and 6 for details).

Once again the RR Lyrae provide an independent check concerning the apparent distance modulus. By summing the $(m - M)_0$ with $3.2 \times E(B - V)$, we estimated $(m - M)_V$ as $17.80^{+0.08}_{-0.09}$. This result is in agreement with the one presented in Section 5.2 within the limit of 1σ confidence interval (see Fig. 9).

BaSTI isochrones essentially confirm the distance and reddening values from the analysis using DSED models. However, the age from BaSTI after the expected correction is somewhat younger than all previous determinations, including those from the same stellar evolutionary models but analysing pure NIR data.

8 DISCUSSION ON AGE AND DISTANCE

From the previous section, it is clear that there is an excellent agreement between the ages and distances for both stellar evolutionary models and both CMDs. Taking into account the atomic diffusion, the average values for the age and distance are $12.8^{+0.9}_{-0.8}$ Gyr and $6.59^{+0.17}_{-0.15}$ kpc. The uncertainties in these values are largely dominated by the formal ones from the MCMC method. The systematics uncertainties, i.e. those due to the different choices of model and CMD, are significantly smaller, as attested by the

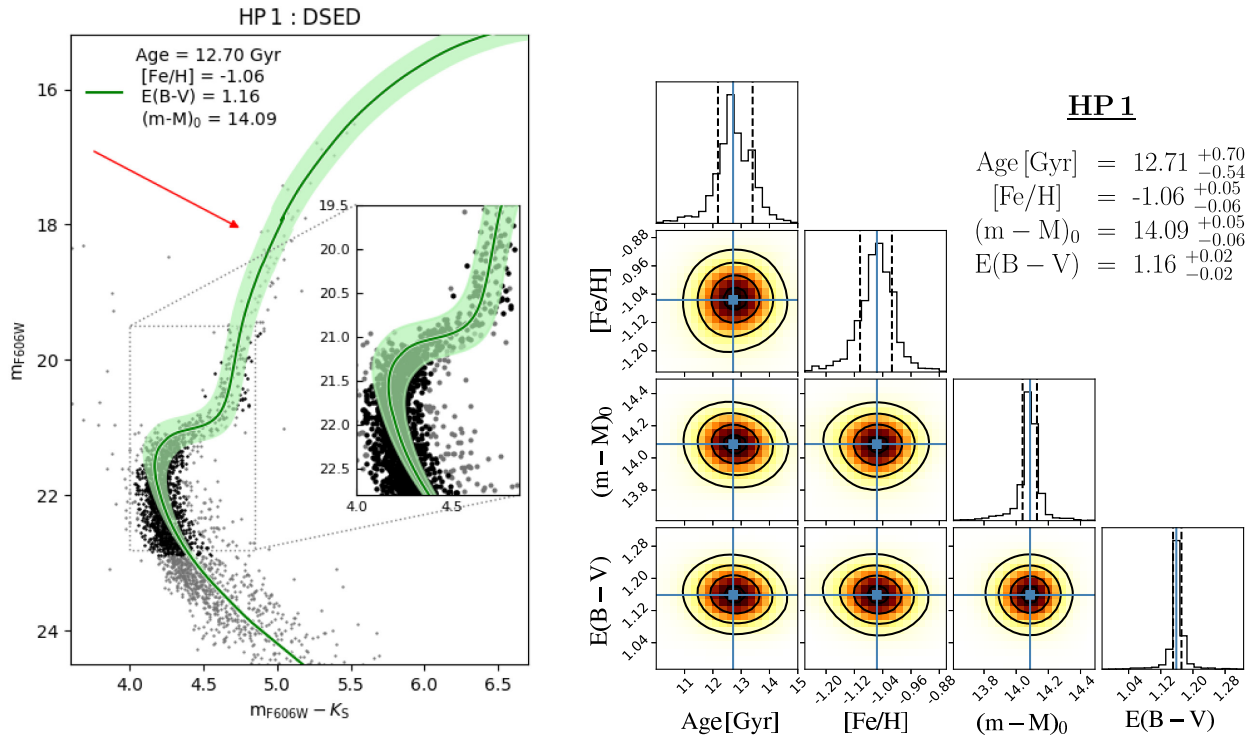

Figure 15. Same as Fig. 13 but for m_{F606W} versus ($m_{F606W} - K_s$) CMD using DSED models and a reddening vector corresponding to $\delta E(B-V) = 0.30$.

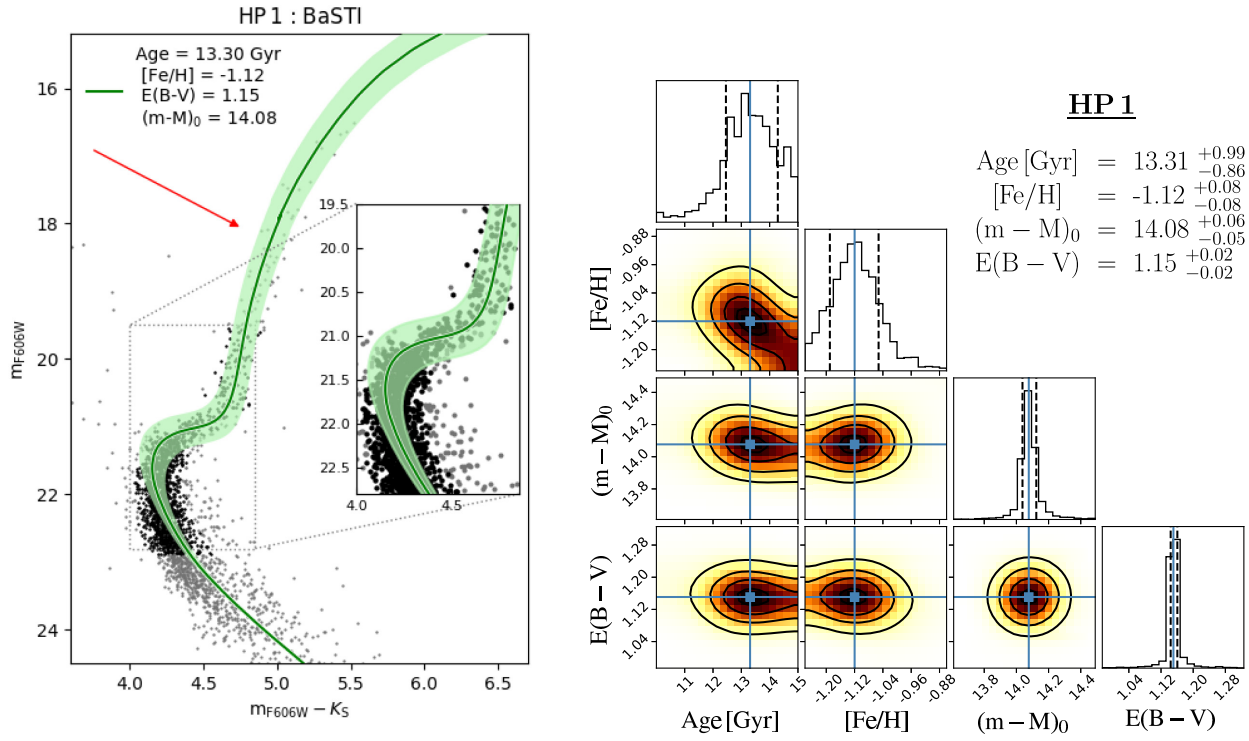

Figure 16. Same as Fig. 15, but for BaSTI models.

standard deviation of the mean over the four determinations (0.2 Gyr and 0.05 kpc).

The absolute ages recovered in this work locate HP 1 as one of the most ancient GCs in our Galaxy, probably formed in the first Gyr of the Universe. This corroborates the hypothesis that relatively metal-poor bulge GCs ([Fe/H] $\lesssim -1.0$) with BHB and α-enhancement can be older than 12.5 Gyr, as very recently demonstrated for NGC 6558 (Barbuy et al. 2018), NGC 6522 and NGC 6626 (Kerber et al. 2018) using optical PM-cleaned CMDs obtained with *HST*. Although metal-poor halo GCs ([Fe/H] ~ -2.0), like M15 (e.g. Monelli et al. 2015), are the most obvious candidates to harbour the oldest stars in the MW, we are demonstrating that a very low metallicity is not a restrictive prior condition to find very old stars in the bulge. In fact, the existence of some GCs with $-1.4 \lesssim$ [Fe/H] $\lesssim -1.0$ and $R_{\rm GC} \lesssim 3.0$ kpc among the oldest GCs was reported by several works using *HST* data (Marín-Franch et al. 2009; Dotter et al. 2010; VandenBerg et al. 2013; Wagner-Kaiser et al. 2017). Furthermore, Dotter et al. (2010) identify the age as the second parameter to explain the HB morphology, being the clusters with BHB the oldest ones. A notable example of such old GC with all aforementioned characteristics is NGC 6717.

In order to compare our derived age results for HP 1, we here discuss two recent papers that determined absolute ages for GCs using deep NIR data collected with GSAOI + GeMS@Gemini-S. Saracino et al. (2016) presented the analysis of a $K_{\rm S}$ versus $(J - K_{\rm S})$ CMD of NGC 6624, a bulge GC with [Fe/H] $= -0.69 \pm 0.02$ and [α/Fe]$\sim+$ 0.39 (Valenti et al. 2011). Using three different stellar evolutionary models, including DSED and BaSTI, they recovered an age of 12.0 $\pm$ 0.5 Gyr, somewhat younger than the one determined by us for HP 1. These authors did not apply the correction for the lack of atomic diffusion in the BaSTI models, therefore overestimating the age of NGC 6624. A similar age of 11.9 $\pm$ 0.7 (intrinsic)$\pm$0.45 (metallicity term) Gyr was determined for NGC 2808 by Massari et al. (2016a), a halo GC with [Fe/H] $= -1.13 \pm 0.04$ (Carretta 2015), i.e. a GC with a metallicity similar to the one of HP 1. Combining the NIR data from GSAOI+GeMS with optical photometry extracted from *HST* images, they estimated the ages computing the difference between the MSTO and the MS knee presented in the NIR. Curiously, NGC 6624 and NGC 2808 present simultaneously blue and red HB stars, as well as remarkable multiple populations when UV and optical *HST* images are employed to build CMDs (Piotto et al. 2015). Furthermore, NGC 2808 presents a complex GC with five distinct stellar populations according to the [Na/Mg] ratios (Carretta 2015; Milone et al. 2015). Despite these features, the stars within each of these clusters have similar ages, probably not so old as the ones in HP 1.

Since we have a very accurate heliocentric distance, directly confirmed from the analysis of RR Lyrae stars in the NIR, we can estimate a Galactocentric distance ($R_{\rm GC}$) for HP 1 only limited by the uncertainties in the distance of the Sun to the Galactic Centre (R_0). Assuming $R_0 = 8.2 \pm 0.2$ kpc from the recent statistical analysis done by Bland-Hawthorn & Gerhard (2016) over 26 independent determinations, we recover a value of $R_{\rm GC} = 1.7 \pm 0.3$ kpc for HP 1.

9 ORBITAL ANALYSIS OF HP 1

We determined a new, accurate (uncertainties $\lesssim$2 per cent) distance of HP 1. We used this distance, combined with the absolute PMs and the radial velocity, of the cluster to refine the orbit of HP 1 computed in Ortolani et al. (2011).

Table 2. HP 1 parameters for the orbit integration.

Parameter	Value	Reference
$(\alpha, \delta)_{(J2000)}$	$(17^{\rm h}31^{\rm m}05^{\rm s}.2, -29^\circ58'54'')$	1
Radial velocity	40 ± 0.5 km s^{-1}	2
$d_\odot$	6.59 ± 0.16 kpc	This work
$\mu_\alpha \cos\delta$	2.409 ± 0.054^a mas yr^{-1}	This work^b
μ_δ	-10.136 ± 0.046^a mas yr^{-1}	This work^b

References: (1) Harris 1996. (2) Barbuy et al. 2016.
[a]Uncertainty includes the systematic error of 0.035 mas yr^{-1}.
[b]Obtained by using Gaia DR2 (Gaia Collaboration et al. 2018).

Our PMs are relative to the bulk motion of the cluster and not in an absolute reference-frame system. Therefore, we made use of the absolute PMs available in the *Gaia* DR2 catalogue (Gaia Collaboration et al. 2016a, 2018) to compute the bulk absolute motion of HP 1.

First, we selected all stars within 0.1 deg from the centre of HP 1 with an absolute PM measurement. Then, we rejected all objects with a poorly measured absolute PM according to the prescriptions given in Arenou et al. (2018). We further refined the sample by considering only stars with an absolute PM error smaller than 0.25 mas yr^{-1}. Finally, we computed the 5σ-clipped median value of the absolute PMs along $\alpha\cos\delta$ and δ directions. We find

$$(\mu_\alpha \cos\delta, \mu_\delta)_{\rm HP\,1} = (2.409 \pm 0.042, -10.136 \pm 0.031) \text{ mas yr}^{-1}.$$

The error bars do not include the systematic error of 0.035 mas yr^{-1} described in Gaia Collaboration et al. (2018). Our PMs are consistent with the PMs determined by Vasiliev (2018) and Baumgardt et al. (2019), both based on *Gaia* DR2 PMs as well.

The registration of our relative PMs in an absolute system was not possible because of the large magnitude difference between our and the *Gaia* catalogues. Therefore, we adopted the *Gaia*-based absolute PMs as input parameter for the orbit computation.

The radial velocity, from high-resolution spectroscopy, adopted for the computation is 40.0 $\pm$ 0.5 km s^{-1} (Barbuy et al. 2016). Interestingly, we found one star with a radial-velocity measurement in the *Gaia* DR2 catalogue that is member of HP1 from the PMs. The radial velocity of this probable HP1 star is 42.25 $\pm$ 2.75 km s^{-1}. This value is in agreement with that computed by Barbuy et al. (2016).

The axisymmetric Galactic model includes a Sérsic bulge, an exponential disc generated by the superposition of three Miyamoto–Nagai potentials (Miyamoto & Nagai 1975), following the methodology made by Smith et al. (2015), and a dark matter halo is modelled with the Navarro–Frenk–White (NFW) density profile (Navarro, Frenk & White 1997), having a circular velocity $V_0 =$ 241 km s^{-1} at $R_0 = 8.2$ kpc (Bland-Hawthorn & Gerhard 2016). For the Galactic bar, we employed a triaxial Ferrer's ellipsoid, where all the mass from the Sérsic bulge component is converted into bar. For the bar potential, we assume a total bar mass of 1.2×10^{10} M$_\odot$, an angle of 25° with the Sun-major axis of the bar, a gradient of pattern speed of the bar $\Omega_{\rm b} = 40$, 45, and 50 km s^{-1} kpc^{-1}, and a major axis extension of 3.5 kpc. Even though we vary the bar angular velocity, we keep the same bar extension. In our Galactic model, we are not taking into account the contribution of the spiral arms, given that HP 1 is confined inside 3 kpc from the Galactic Centre, therefore the spiral arms would have a negligible effect.

The integration of the orbits was made with the `NIGO` tool (Rossi 2015a), which includes the potentials mentioned above. The

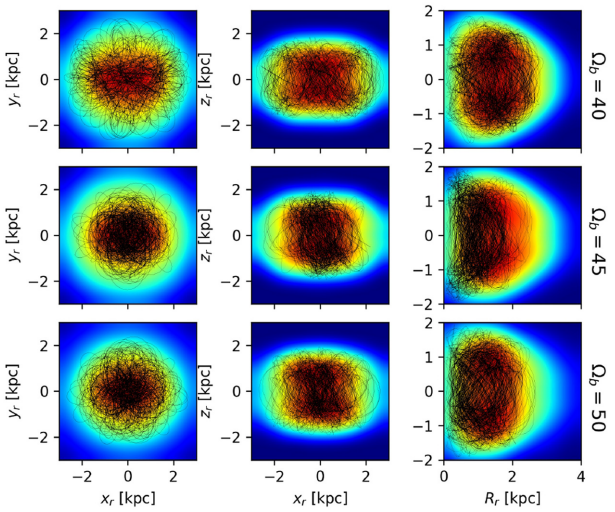

Figure 17. Probability density map for the $x_r - y_r$ (left-hand panels), $x_r - z_r$ (middle panels), and $R_r - z_r$ (right-hand panels) projections of the 1000 Orbits for HP 1 co-rotating with the bar frame, with a gradient in the angular velocity of the Galactic bar: 40 (top row), 45 (middle row), and 50 (bottom row) km s^{-1} kpc^{-1}. The black lines show the orbits using the central values given in Table 2.

solution of the equations of motion is evaluated numerically using the Shampine–Gordon algorithm (for details, see Rossi 2015b). We adopted the right-handed, Galactocentric Cartesian system, x towards the Galactic Centre, and z towards the Galactic North Pole. The initial conditions of the cluster is obtained from the observational data, coordinates, heliocentric distance, radial velocity, and absolute proper motions given in Table 2. The velocity components of the Sun with respect to the local standard of rest are $(U, V, W)_\odot = (11.1, 12.24, 7.25)$ km s^{-1} (Schönrich, Binney & Dehnen 2010). In order to evaluate, the effect of the uncertainties associated with the HP 1's parameters, we employ the Monte Carlo method to generate a set of 1000 initial conditions taking into account the errors of distance, heliocentric radial velocity and absolute proper motion components. We integrate the orbits with such initial conditions forwards for 10 Gyr. For each orbit, we calculate the perigalactic distance $r_{\rm min}$, apogalactic distance $r_{\rm max}$, the maximum vertical distance from the Galactic plane $|z|_{\rm max}$, and the eccentricity defined by $e = (r_{\rm max} - r_{\rm min})/(r_{\rm max} + r_{\rm min})$.

Fig. 17 shows the probability densities of the orbits of HP 1, in the frame co-rotating with the bar. For each value of angular velocity we analysed, we show the $x_r - y_r$, $x_r - z_r$, and $R_r - z_r$ projections (different rows). The red and yellow colours highlight the space region that the orbits cross more frequently. The orbit with central values given in Table 2 (black curve) is confined in the inner region of the Galaxy, inside 3 kpc, having a boxy-shape orbit in $x_r - z_r$ projection with an almost negligible dependence of the angular velocity. This kind of orbits give the orbital support to the X-shape in the Galactic bulge (Portail, Wegg & Gerhard 2015). For the case of $\Omega_{\rm b} = 40$ km s^{-1} kpc^{-1}, the orbit reaches closer to the Galactic Centre. Additionally, we calculate the z-angular momentum in the inertial reference frame, Lz, with the purpose of checking its sign, given that Lz is not conserved, to determine the sense of motion of HP 1 orbit. We found that the orbit of HP 1 has prograde and retrograde motion at the same time. This has been connected with chaotic behaviour (Pichardo, Martos & Moreno 2004).

Distributions for the perigalactic distance, apogalactic distance, maximum vertical height, and the eccentricity are presented in Fig. 18, the different colours represent the angular velocities we investigated. The orbits of HP 1 have radial excursions between ∼0.1 and ∼4.0 kpc, with maximum vertical excursions from the Galactic plane between ∼1.5 and ∼2.1 kpc, and eccentricities $e > 0.8$. The variation of the angular velocity seems to have an insignificant effect on the orbits. In Table 3, we present average orbital parameters of the set of orbits for HP 1, the errors provide in each column are the standard deviation of the distribution. Baumgardt et al. (2019) also used *Gaia* DR2 PMs to integrate the orbit of HP 1 and calculate their perigalactic and apogalactic distances, 0.56 and 1.95 kpc, respectively. The differences with our orbital calculations are possibly due to the facts that they integrate backwards for 2 Gyr only, in an axisymmetric Galactic potential, and the heliocentric distance is ∼200 pc farther than our distance determination.

The orbital characteristics of HP 1 are consistent with the bulge GCs that have [Fe/H] ∼ −1.0 (Pérez-Villegas et al. 2018), being well confined to the Galactic volume where bulge GCs are located, $R_{\rm GC} \leq 3.0$ kpc (Bica, Ortolani & Barbuy 2016).

10 SUMMARY AND CONCLUSIONS

We obtained unprecedented deep NIR photometry in the crowded field of the moderately metal-poor ([Fe/H] = −1.06 ± 0.10) and α-enhanced ([α/Fe]∼+ 0.3) inner bulge GC HP 1. The GSAOI + GeMS detector at the Gemini-South telescope provides an unique opportunity to obtain MCAO images in J and $K_{\rm S}$ filters. By combining our GSAOI data with archival *HST* exposures, we computed the relative PMs of the stars in the core of HP 1 and infer their membership to the cluster. This way, we created NIR and optical-NIR CMDs down to $K_{\rm S} \sim 19.5$ with only likely cluster members to analyse.

A statistical isochrone fitting technique following a Bayesian approach was employed to determine ages, distances and reddening in a self-consistent way. For this purpose, we used DSED and BaSTI α-enhanced isochrones with canonical helium abundances ($Y \sim 0.25$). Furthermore, a sample of 11 RR Lyrae stars (from the OGLE CVS, Soszyński et al. 2014, but also identified in the VVV survey, Saito et al. 2012) and a colour–colour diagram ($m_{\rm F606W} - K_{\rm S}$ versus $J - K_{\rm S}$) were used to provide independent constraints for the distance, reddening, and helium content. The main results from the isochrone fits can be summarized as follow:

(i) The NIR and optical-NIR CMDs using DSED and BaSTI models confirm that HP 1 is a fossil relic with an age of $12.8^{+0.9}_{-0.8}$ Gyr.

(ii) The heliocentric and Galactocentric distances for this cluster are $6.59^{+0.17}_{-0.15}$ kpc and 1.7 ± 0.3 kpc, respectively.

(iii) The apparent distance moduli in $K_{\rm S}$ and V are in very good agreement with the ones from the RR Lyrae stars using the recent $PM_{K_{\rm S}}Z$ and M_V −[Fe/H] calibrations provided by the Gaia Collaboration (2017).

(iv) A primordial He content is imposed by the mean magnitude of the RR Lyrae stars, otherwise the heliocentric cluster distance should be unrealistically high.

(v) The $E(B - V)$ of HP 1 is 1.15 ± 0.02, with good concordance between all isochrone fits.

(vi) Even assuming uniform prior probability distributions, the recovered metallicity values are in very good agreement with the

Table 3. Monte Carlo average orbital parameters of HP 1.

Ω_b	$\langle r_{\rm min}\rangle$	$\langle r_{\rm max}\rangle$	$\langle \lvert z\rvert_{\rm max}\rangle$	$\langle e\rangle$
(km s^{-1} kpc^{-1})	(kpc)	(kpc)	(kpc)	
40	0.128 ± 0.079	3.076 ± 0.350	1.841 ± 0.104	0.922 ± 0.040
45	0.124 ± 0.070	3.125 ± 0.404	1.843 ± 0.114	0.924 ± 0.037
50	0.119 ± 0.050	3.064 ± 0.460	1.861 ± 0.116	0.925 ± 0.031

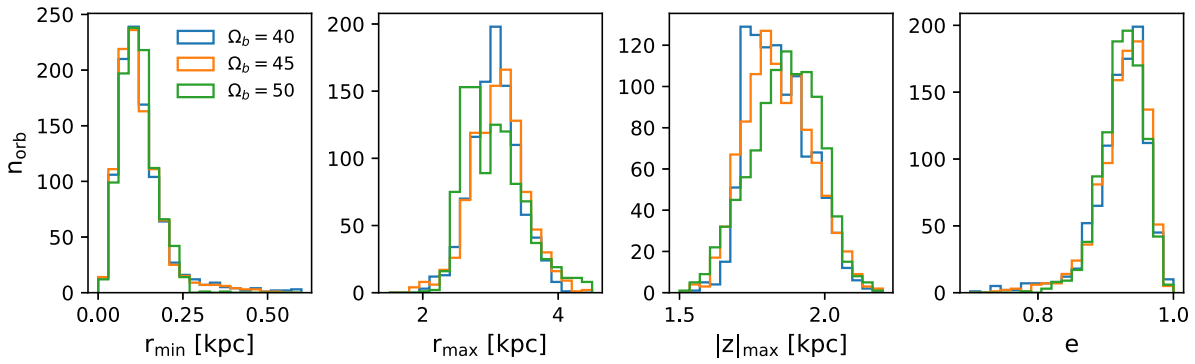

Figure 18. Distribution of orbital parameters for HP 1, perigalactic distance $r_{\rm min}$, apogalactic distance $r_{\rm max}$, maximum vertical excursion from the Galactic plane $|z|_{\rm max}$, and eccentricity. The colours show the different angular speed of the bar, $\Omega_{\rm b} = 40$ (blue), 45 (orange), and 50 (green) km s^{-1} kpc^{-1}.

one from high- resolution spectroscopy (Barbuy et al. 2016), adding reliability to the aforementioned results.

We also performed an orbital analysis for HP 1, taking into account the uncertainties of its parameters, through a Monte Carlo method. We found that the HP 1's orbit is typical for moderately metal-poor bulge GCs, with apogalactic distances not farther than ∼4 kpc. These orbits present an average apogalactic distance $\langle r_{\rm max}\rangle = 3.1 \pm 0.4$ kpc, which can be considered as a representative distance where it is possible to find fossil relics of the early fast chemical enrichment in the Galactic bulge.

To establish a comprehensive scenario about the formation of the MW bulge, an homogeneous statistical analysis applied to a large sample of bulge GCs with deep NIR PM-cleaned CMDs is highly recommended.

ACKNOWLEDGEMENTS

We are thankful to the anonymous referee for a careful reading and useful suggestions. LK, BB, and EB acknowledge partial financial support from FAPESP, CNPq, and CAPES – Finance Code 001. RAPO acknowledges a CAPES master fellowship and SOS a FAPESP IC fellowship 2016/20566-7. ML, SO, and DN acknowledge partial support by the Dipartimento di Fisica e Astronomia dell'Università di Padova. APV acknowledges FAPESP for the postdoctoral fellowship 2017/15893-1. APV acknowledges DGAPA PAPIIT IG100319.

This study was based on observations obtained at the Gemini Observatory, which is operated by the Association of Universities for Research in Astronomy, Inc., under a cooperative agreement with the NSF on behalf of the Gemini partnership: the National Science Foundation (United States), National Research Council (Canada), CONICYT (Chile), Ministerio de Ciencia, Tecnología e Innovación Productiva (Argentina), Ministério da Ciência, Tecnologia e Inovação (Brazil), and Korea Astronomy and Space Science Institute (Republic of Korea).

This study was also based on observations made with the NASA/ESA Hubble Space Telescope, obtained from the data archive at the Space Telescope Science Institute. STScI is operated by the Association of Universities for Research in Astronomy, Inc. under NASA contract NAS 5-26555.

REFERENCES

Alves V. M., Pavani D. B., Kerber L. O., Bica E., 2012, New Astron., 17, 488
Anderson J., Bedin L. R., 2010, PASP, 122, 1035
Anderson J., King I. R., 2006, ACS/ISR 2006-01 (Baltimore, MD: STScI). Available online at http://www.stsci.edu/hst/acs/documents/isrs
Anderson J., King I. R., 2003, PASP, 115, 113
Anderson J., King I. R., 2004, Instrument Science Report ACS 2004-15, 51 pages, 3
Anderson J., Bedin L. R., Piotto G., Yadav R. S., Bellini A., 2006, A&A, 454, 1029
Anderson J. et al., 2008a, AJ, 135, 2055
Anderson J. et al., 2008b, AJ, 135, 2114
Arenou F. et al., 2018, A&A, 616, A17
Barbuy B. et al., 2016, A&A, 591, A53
Barbuy B., Bica E., Ortolani S., 1998, A&A, 333, 117
Barbuy B. et al., 2006, A&A, 449, 349
Barbuy B., Zoccali M., Ortolani S., Minniti D., Hill V., Renzini A., Bica E., Gómez A., 2007, AJ, 134, 1613
Barbuy B., Zoccali M., Ortolani S., Hill V., Minniti D., Bica E., Renzini A., Gómez A., 2009, A&A, 507, 405
Barbuy B. et al., 2014, A&A, 570, A76
Barbuy B. et al., 2018, A&A, 619, A178
Baumgardt H., Hilker M., Sollima A., Bellini A., 2019, MNRAS, 482, 5138
Beaton R. L. et al., 2016, ApJ, 832, 210
Bellini A., Bedin L. R., 2009, PASP, 121, 1419
Bellini A., Bedin L. R., 2010, A&A, 517, A34
Bellini A., Anderson J., Bedin L. R., 2011, PASP, 123, 622
Bellini A., Anderson J., Bedin L. R., King I. R., van der Marel R. P., Piotto G., Cool A., 2017a, ApJ, 842, 6

Bellini A., Anderson J., van der Marel R. P., King I. R., Piotto G., Bedin L. R., 2017b, ApJ, 842, 7
Bellini A. et al., 2018, ApJ, 853, 86
Bessell M. S., Brett J. M., 1988, PASP, 100, 1134
Bica E., Ortolani S., Barbuy B., 2016, PASA, 33, 28
Bland-Hawthorn J., Gerhard O., 2016, ARA&A, 54, 529
Bressan A., Marigo P., Girardi L., Salasnich B., Dal Cero C., Rubele S., Nanni A., 2012, MNRAS, 427, 127
Carretta E., 2015, ApJ, 810, 148
Cassisi S., Castellani V., degl'Innocenti S., Weiss A., 1998, A&AS, 129, 267
Cassisi S., Castellani V., degl'Innocenti S., Salaris M., Weiss A., 1999, A&AS, 134, 103
Cescutti G., Matteucci F., Lanfranchi G. A., McWilliam A., 2008, A&A, 491, 401
Cohen R. E., Moni Bidin C., Mauro F., Bonatto C., Geisler D., 2017, MNRAS, 464, 1874
Cohen R. E., Mauro F., Alonso-García J., Hempel M., Sarajedini A., Ordoñez A. J., Geisler D., Kalirai J. S., 2018, AJ, 156, 41
Dalessandro E. et al., 2016, ApJ, 833, 111
Dias B., Barbuy B., Saviane I., Held E. V., Da Costa G. S., Ortolani S., Gullieuszik M., Vásquez S., 2016a, A&A, 590, A9
Dias B., Kerber L., Barbuy B., Bica E., Ortolani S., 2016b, A&A, 591, A11
Dotter A., Chaboyer B., Jevremović D., Kostov V., Baron E., Ferguson J. W., 2008, ApJS, 178, 89
Dotter A. et al., 2010, ApJ, 708, 698
Ferraro F. R., Massari D., Dalessandro E., Lanzoni B., Origlia L., Rich R. M., Mucciarelli A., 2016, ApJ, 828, 75
Foreman-Mackey D., 2016, J. Open Source Softw., 1, 24
Foreman-Mackey D., Hogg D. W., Lang D., Goodman J., 2013, PASP, 125, 306
Gaia Collaboration et al., 2016a, A&A, 595, A1
Gaia Collaboration et al., 2016b, A&A, 595, A2
Gaia Collaboration et al., 2017, A&A, 605, A79
Gaia Collaboration et al., 2018, A&A, 616, A1
Girardi L. et al., 2008, PASP, 120, 583
Gratton R. G. et al., 2015, A&A, 573, A92
Harris W. E., 1996, AJ, 112, 1487
Hernandez X., Valls-Gabaud D., 2008, MNRAS, 383, 1603
Kerber L. O., Nardiello D., Ortolani S., Barbuy B., Bica E., Cassisi S., Libralato M., Vieira R. G., 2018, ApJ, 853, 15
Lagioia E. P. et al., 2018, MNRAS, 475, 4088
Lee J.-W., Carney B. W., Balachandran S. C., 2004, AJ, 128, 2388
Libralato M., Bellini A., Bedin L. R., Piotto G., Platais I., Kissler-Patig M., Milone A. P., 2014, A&A, 563, A80
Libralato M. et al., 2015, MNRAS, 450, 1664
Marín-Franch A. et al., 2009, ApJ, 694, 1498
Massari D., Lascaux F., Turchi A., Fini L., 2016b, SPIE, 9909, 99091G
Massari D., Bellini A., Ferraro F. R., van der Marel R. P., Anderson J., Dalessandro E., Lanzoni B., 2013, ApJ, 779, 81
Massari D. et al., 2016a, A&A, 595, L2
McCall M. L., 2004, AJ, 128, 2144
Milone A. P. et al., 2012, A&A, 540, A16
Milone A. P. et al., 2015, ApJ, 808, 51
Milone A. P. et al., 2018, MNRAS, 481, 5098
Minniti D. et al., 2010, New A, 15, 433
Minniti D. et al., 2017, ApJ, 849, L24
Miyamoto M., Nagai R., 1975, PASJ, 27, 533
Monelli M. et al., 2015, ApJ, 812, 25
Monteiro H., Dias W. S., Caetano T. C., 2010, A&A, 516, A2
Muñoz C., Villanova S., Geisler D., Saviane I., Dias B., Cohen R. E., Mauro F., 2017, A&A, 605, A12
Nardiello D. et al., 2015, MNRAS, 451, 312
Navarro J. F., Frenk C. S., White S. D. M., 1997, ApJ, 490, 493
Naylor T., Jeffries R. D., 2006, MNRAS, 373, 1251
Origlia L., Rich R. M., 2004, AJ, 127, 3422
Ortolani S., Bica E., Barbuy B., 1997, MNRAS, 284, 692
Ortolani S., Barbuy B., Momany Y., Saviane I., Bica E., Jilkova L., Salerno G. M., Jungwiert B., 2011, ApJ, 737, 31
Pérez-Villegas A., Rossi L., Ortolani S., Casotto S., Barbuy B., Bica E., 2018, PASA, 35, 21
Perren G. I., Piatti A. E., Vázquez R. A., 2017, A&A, 602, A89
Pichardo B., Martos M., Moreno E., 2004, ApJ, 609, 144
Pieres A. et al., 2016, MNRAS, 461, 519
Pietrinferni A., Cassisi S., Salaris M., Castelli F., 2006, ApJ, 642, 797
Piotto G. et al., 2015, AJ, 149, 91
Planck CollaborationXIII, 2016, A&A, 594, A13
Portail M., Wegg C., Gerhard O., 2015, MNRAS, 450, L66
Rossi L. J., 2015a, Astrophysics Source Code Library, record ascl: 1501.002
Rossi L. J., 2015b, Astron. Comput., 12, 11
Rossi L. J., Ortolani S., Barbuy B., Bica E., Bonfanti A., 2015, MNRAS, 450, 3270
Saito R. K. et al., 2012, A&A, 544, A147
Saracino S. et al., 2015, ApJ, 806, 152
Saracino S. et al., 2016, ApJ, 832, 48
Sarajedini A. et al., 2007, AJ, 133, 1658
Schiavon R. P. et al., 2017, MNRAS, 466, 1010
Schönrich R., Binney J., Dehnen W., 2010, MNRAS, 403, 1829
Skrutskie M. F. et al., 2006, AJ, 131, 1163
Smith R., Flynn C., Candlish G. N., Fellhauer M., Gibson B. K., 2015, MNRAS, 448, 2934
Soszyński I. et al., 2014, Acta Astron., 64, 17
Turri P., McConnachie A. W., Stetson P. B., Fiorentino G., Andersen D. R., Véran J.-P., Bono G., 2015, ApJ, 811, L15
Valenti E., Ferraro F. R., Origlia L., 2007, AJ, 133, 1287
Valenti E., Ferraro F. R., Origlia L., 2010, MNRAS, 402, 1729
Valenti E., Origlia L., Rich R. M., 2011, MNRAS, 414, 2690
VandenBerg D. A., Brogaard K., Leaman R., Casagrande L., 2013, ApJ, 775, 134
Vasiliev E., 2018, preprint (arXiv:1807.09775)
Villanova S., Moni Bidin C., Mauro F., Munoz C., Monaco L., 2017, MNRAS, 464, 2730
Wagner-Kaiser R., Sarajedini A., von Hippel T., 2017, MNRAS, 468, 1038

APPENDIX: GEOMETRIC DISTORTION

The GD of GSAOI has been solved by different authors, e.g. Massari et al. (2016b) and Dalessandro et al. (2016), with different techniques. In this paper, we followed the prescriptions given by Anderson & King (2003, 2004), Bellini & Bedin (2009, 2010), Bellini, Anderson & Bedin (2011), and Libralato et al. (2014, 2015). Note that the AO-induced changes of the mirror configuration are expected to make the incoming light reaching the detector through a different path in each image (e.g. Massari et al. 2016b). As such, the GD is expected to slightly change from image to image and our GD solution is meant to be an average GD solution.

The data set employed to solve for the GD of GSAOI is that of the GC NGC 6624 (programme GS-2013A-Q23, PI: D. Geisler), which was also adopted by Dalessandro et al. (2016) for the same GD-correction task. This data set was obtained when the GC was close to the zenith, with optimal and stable seeing conditions. The dither pattern of these observations is not ideal for a GD self-calibration (see discussion in Libralato et al. 2014), but it is large enough to allow us to calibrate the GD on to an external, distortion-free reference frame.

As Dalessandro et al. (2016), we chose a *HST* catalogue to use as reference. We adopted the public-available,[9] preliminary-release catalogue of the '*Hubble Space Telescope* UV Legacy

[9] http://groups.dfa.unipd.it/ESPG/treasury.php

Survey of Galactic GCs' (GO-13297, PI: G. Piotto, see Piotto et al. 2015). Stellar positions are those listed in the ACS Globular Cluster Treasury Survey catalogue (GO-10775, PI: A. Sarajedini, see Anderson et al. 2008a).

In our GD analysis, we considered only stars members of NGC 6624 to avoid relative PMs (GSAOI images were obtained 7 years after *HST* data) to mask out the systematic GD trends with an amplitude lower than that induced by the relative cluster-field motion. At this aim, we made advantage of stellar displacements available in this release of the catalogue obtained by combining the ACS Treasury and the UV Legacy Survey data.

The GD correction was performed independently for each chip by means of a third-order polynomial. As in Anderson & King (2003) and Bellini & Bedin (2010), we adopted the centre of each chip (x, y) = (1024,1024) as reference pixel with respect to which solve for the GD.

First, we selected bright, unsaturated, well-measured (QFIT< 0.05) stars in each GSAOI catalogue. Then, we transformed stellar positions from the *HST* reference frame (hereafter master frame) on to the reference frame of each chip/image. We adopted four-parameter linear transformations (rigid shifts in the two coordinates, one rotation, and one change of scale) to bring the stellar position from one frame to the other. Positional residuals were computed as the difference between the distortion-free, master-frame-transformed positions and the GSAOI positions.

For each chip, stellar positional residuals were collected into a 16 × 16 look-up table (grid elements of 128 × 128 GSAOI pixel^2 each). We then computed the 3σ-clipped average value of the residuals in each cell. Finally, we calculated the coefficients of the third-order polynomial with a linear least-square fit to the average residuals.

GSAOI positions were corrected for GD by using the available third-order polynomial correction. The entire procedure was iterated, each time computing new, improved linear transformations between the master frame and the GD-corrected GSAOI catalogues, and new positional residuals to refine the coefficients of the third-order polynomials. The iterations ceased when the difference between the polynomial coefficients from one iteration to the previous one was negligible.

Dalessandro et al. (2016) solved for the GD of GSAOI detector with a procedure similar to that described here. The main difference with the work of Dalessandro et al. is that we set the coefficients a_1 and a_2 of their equation (3) equal to zero. As discussed in, e.g. Anderson & King (2003) and Bellini & Bedin (2010), this convention constraints the GD solution to have at the centre of the chip (i) the x-scale equal to that of the chip at the position of the reference pixel, and (ii) the y-axis in the GD-corrected frame aligned to its y-axis (always at the position of the reference pixel). The coefficients b_1 and b_2 of their equation (4) were left free to assume any value from the fit because the scale and the perpendicularity of the two axes can be different.

The K_S- and J-filter distortion maps before and after the GD correction are shown in Figs A1 and A2, respectively. In Fig. A3, we present the σ (Radial residuals) as a function of instrumental magnitude for K_S- (left) and J-filter (right) data after each step of the GD correction. The σ(Radial residuals), computed as described in Libralato et al. (2014, 2015), is indicative of the accuracy of our GD solution. This value is defined as the rms of the difference between the master-frame positions and the GD-corrected stellar positions as measured in a given image transformed on to the master-frame system. The master frame used for this computation is not the *HST* catalogue, but it was obtained by cross-identifying the same stars in the GSAOI catalogues. We find that for bright, well-measured stars, the median value of the σ(Radial residuals) in the K_S-filter data improves from ∼19.8 to 0.52 mas (0.026 GSAOI pixel) in each coordinate. When we use six-parameter linear transformations (that absorb most of the residuals due to the variation of the telescope+optics system) to transform stellar positions from the reference frame of a given catalogue on to the master frame, the value of σ(Radial residuals) further improves to 0.32 mas. For J-filter data, we measure instead a median σ(Radial residuals) of ∼0.44 mas.

We also put the four GSAOI chips into a common, distortion-free reference frame, hereafter meta catalogue, with the same procedure described in Bellini & Bedin (2010). In a nutshell, we transformed the GD-corrected positions of each chip k into the GD-corrected system of chip 2 by means of four-parameter linear transformations. The relations between the positions of a star in the chip-k system ($x_k^{\rm corr}$, $y_k^{\rm corr}$) and that in the chip-2 system ($x_2^{\rm corr}$, $y_2^{\rm corr}$) are the following:

$$\begin{pmatrix} x_2^{\rm corr} \\ y_2^{\rm corr} \end{pmatrix} = \frac{\alpha_k}{\alpha_2} \begin{bmatrix} \cos(\theta_k - \theta_2) & -\sin(\theta_k - \theta_2) \\ \sin(\theta_k - \theta_2) & \cos(\theta_k - \theta_2) \end{bmatrix} \begin{pmatrix} x_k^{\rm corr} - 1024 \\ y_k^{\rm corr} - 1024 \end{pmatrix} + \begin{pmatrix} (x_2^{\rm corr})_k \\ (y_2^{\rm corr})_k \end{pmatrix}.$$

The scale factor is indicated as α_k, the orientation angle as θ_k, and the position of the centre of chip k in the reference frame of chip 2 as $(x_2^{\rm corr})_k$ and $(y_2^{\rm corr})_k$, respectively. By construction, positions in the chip-2 and in the meta systems are the same.

The values of α_k, θ_k, $(x_2^{\rm corr})_k$, and $(y_2^{\rm corr})_k$ in each K_S-filter image are shown in Fig. A4. The final values adopted for the K_S-filter meta solution were computed as the median values of these parameters (see Table A1).

Finally, we investigated how these parameters change by adopting a different filter. We performed the same computation with the J-filter data and the values are presented in Table A2. The most relevant difference is relative scales. This discrepancy is related to the different optical path introduced by the J filter.

The σ(Radial residuals) obtained by using the meta GD solution is of the order of 0.46 and 0.7 mas for K_S- and J-filter data (the bottom panels of Fig. A3), respectively. The accuracy of the meta solution is slightly worse than the single-chip correction because of the additional uncertainties in the linear terms of the GD. Despite this worse accuracy, the distortion-free meta catalogues can be useful when there are not enough stars to cross-identify all chips (e.g. small-absent dither in the observations or sparse fields).

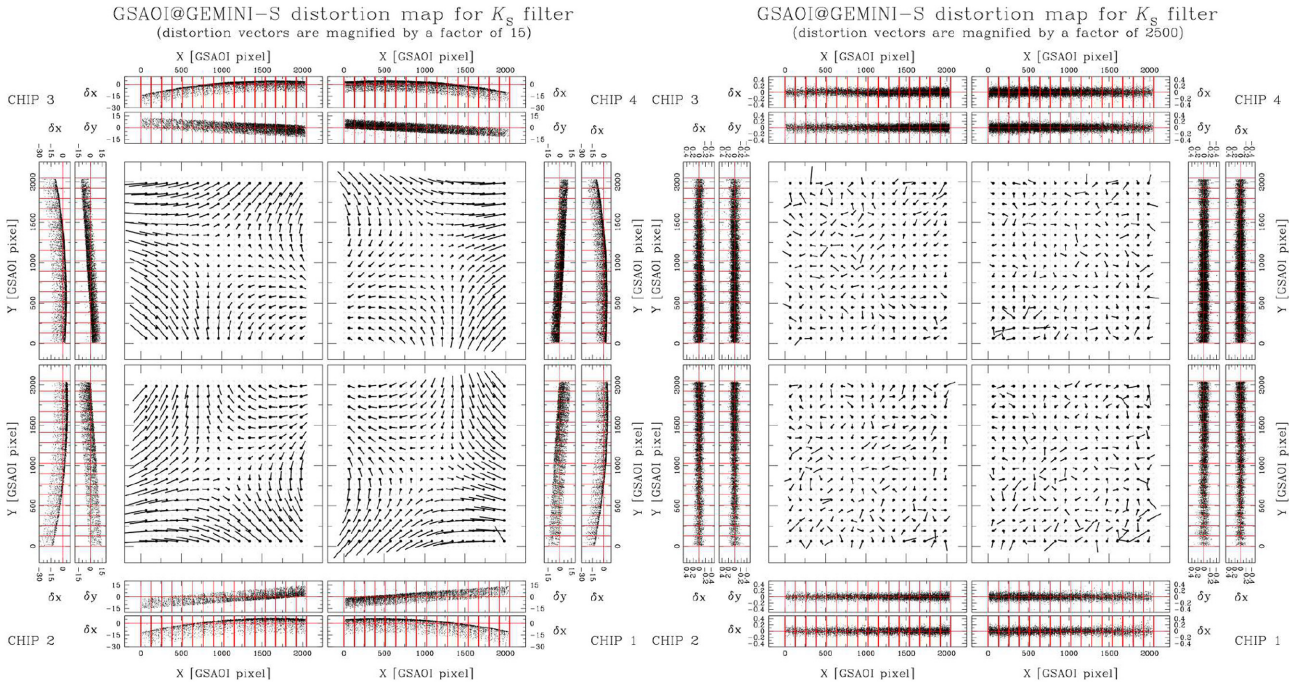

Figure A1 GSAOI K_S-filter distortion maps before (left-hand panels) and after (right-hand panel) applying the GD correction. In the panels outside the distortion maps, we present the $\delta x/\delta y$ positional residuals (in GSAOI pixel) as a function of the x and y positions.

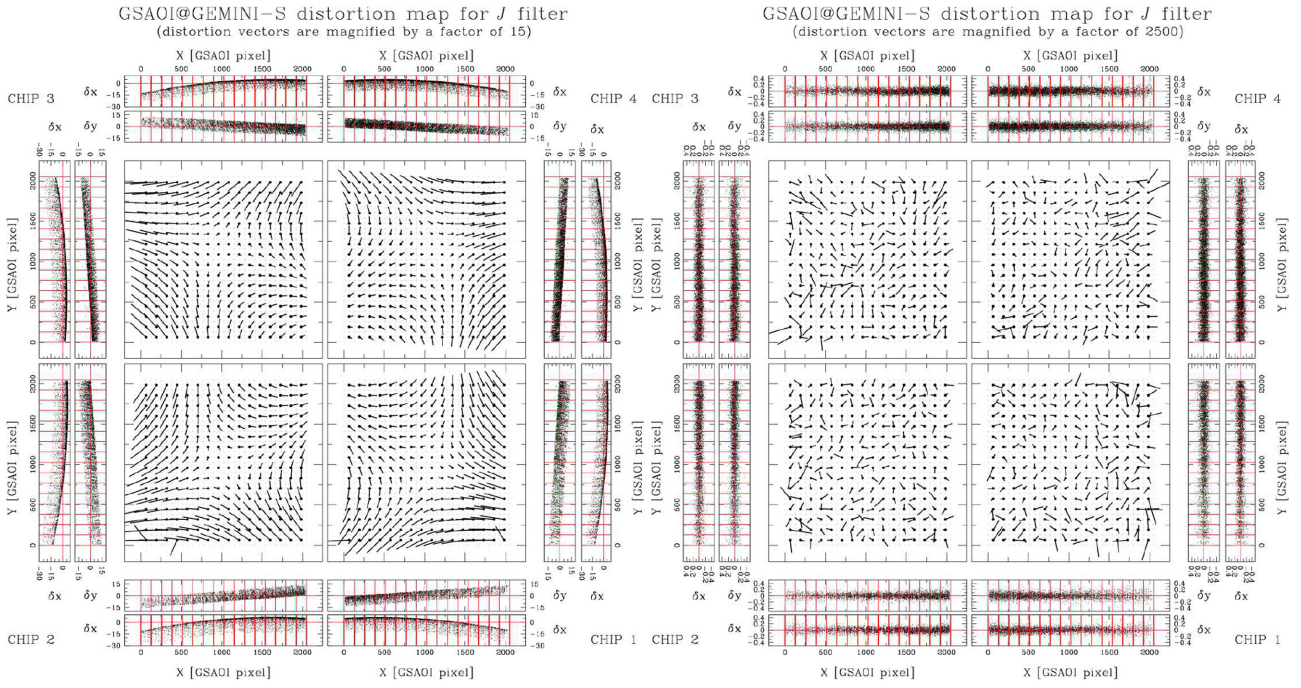

Figure A2 Same as in Fig. A2 but for the J filter data.

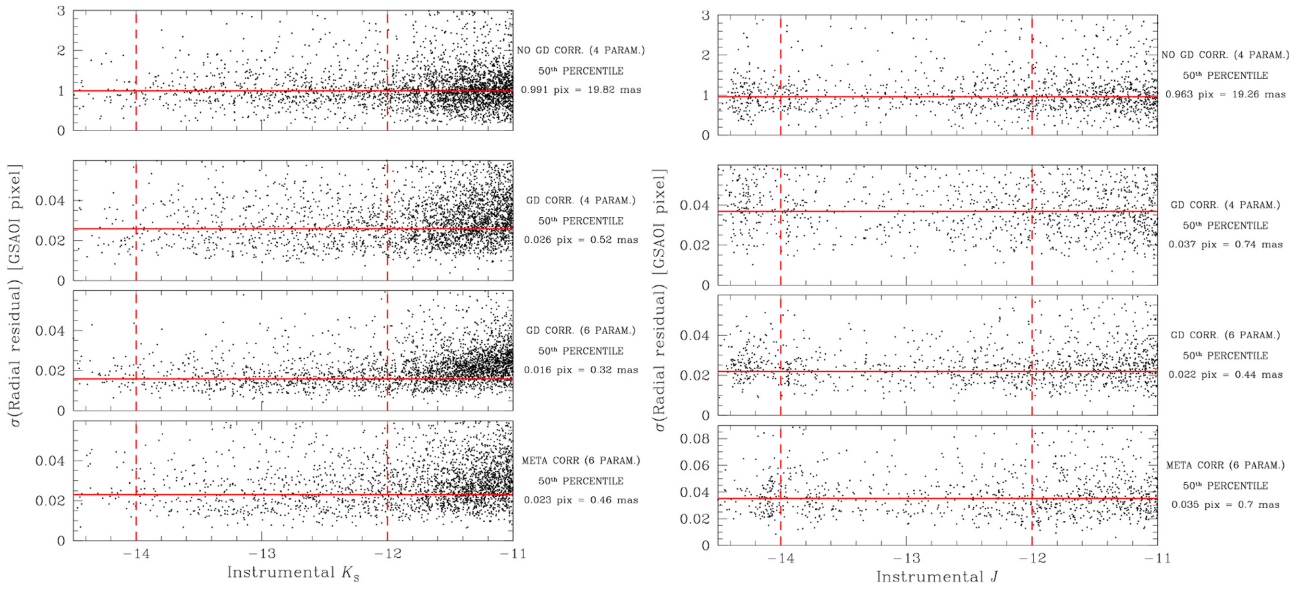

Figure A3 σ(Radial residuals) as a function of K_S (left-hand panels) and J (right-hand panels) instrumental magnitudes after each step of the GD correction. The red, solid horizontal line is set at the median value of σ(Radial residuals) for bright, unsaturated stars (between the two red, dashed vertical lines). In the bottom panels, we present the result obtained by adopting the meta-catalogue solution.

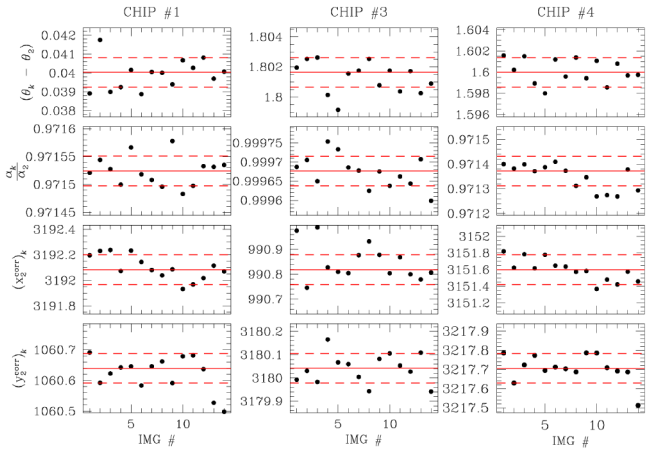

Figure A4 From top to bottom, we present the relative angle (in degrees), scale, x and y positions (in GSAOI pixels) of the central pixel of chip 1 (left column), 3 (middle column), and 4 (right column) with respect to chip 2 of the K_S-filter images. The red, solid horizontal line is the median value of each parameter, the dashed lines are the $\pm 1\sigma$ uncertainties.

Table A1. Relative angle, scale, and central-pixel positions of each chip relative to chip 2 obtained by using the K_S-filter data.

Chip	$\theta_k - \theta_2$ (deg)	α_k/α_2	$(x_2^{corr})_k$ (GSAOI pixel)	$(y_2^{corr})_k$ (GSAOI pixel)
1	0.0400 ± 0.0008	0.97152 ± 0.00003	3192.08 ± 0.12	1060.64 ± 0.05
2	0.0000	1.00000	1024.00	1024.00
3	1.8016 ± 0.0010	0.99968 ± 0.00004	990.82 ± 0.06	3180.04 ± 0.06
4	1.6000 ± 0.0014	0.97137 ± 0.00006	3151.60 ± 0.18	3217.71 ± 0.08

Table A2. As in Table A1 but computed by using the *J*-filter images.

Chip	$\theta_k - \theta_2$ (deg)	α_k/α_2	$(x_2^{\rm corr})_k$ (GSAOI pixel)	$(y_2^{\rm corr})_k$ (GSAOI pixel)
1	0.0435 ± 0.0009	0.97146 ± 0.00004	3192.00 ± 0.11	1060.66 ± 0.13
2	0.0000	1.00000	1024.00	1024.00
3	1.8043 ± 0.0018	0.99955 ± 0.00003	990.82 ± 0.06	3180.03 ± 0.06
4	1.6051 ± 0.0027	0.97137 ± 0.00005	3151.40 ± 0.15	3217.73 ± 0.11

This paper has been typeset from a TEX/LATEX file prepared by the author.